Agricultural and Forest Meteorology 339 (2023) 109557

Contents lists available at ScienceDirect

Agricultural and Forest Meteorology

journal homepage: www.elsevier.com/locate/agrformet

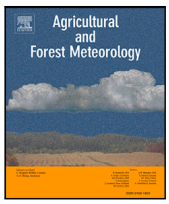

Characterisation of flow dynamics within and around an isolated forest, through measurements and numerical simulations

Carlo Cintolesi [a], Francesco Barbano [a,*], Pier Luigi Trudu [a], Angelo Finco [b], Giacomo Gerosa [b], Silvana Di Sabatino [a]

[a] University of Bologna, Department of Physics and Astronomy, via Irnerio 46, 40126 Bologna, Italy
[b] Università Cattolica del Sacro Cuore, Department of Mathematics and Physics, Via della Garzetta 48, 25133 Brescia, Italy

ARTICLE INFO

Keywords:
Forest canopy flow
Finite forest
Non-homogeneous forest canopy
RANS simulation
Quadrant analysis
OpenFOAM

ABSTRACT

The case study of 'Bosco Fontana', a densely-vegetated forest located in the north of Italy, is analysed both experimentally and numerically to characterise the internal ventilation of a finite forest with a vertically non-homogeneous canopy. Measurements allow for the evaluation of the turbulent exchange across the forest canopy. The case study is then reproduced numerically via a two-dimensional RANS simulation, successfully validated against experimental data. The analysis of the internal ventilation leads to the identification of seven regions of motion along the predominate-wind direction, for whose definition a new in-canopy stability parameter was introduced. In the vertical direction, the non-homogeneity of the canopy leads to the separation of the canopy layer into an upper foliage layer and a lower bush layer, characterised respectively by an increasing streamwise velocity and turbulence intensity, and a weak backflow. The conclusions report an improved description of the dynamic layer and regions of motion presented in the literature.

1. Introduction

Understanding forest ventilation, the in-forest air dynamics and the exchanges with the sounding atmosphere, is crucial for multiple applications due to the impacts of vegetation canopies on the atmospheric flows. After the cornerstone work of Cionco (1965), the characteristics of both mean flows and turbulent structures in vegetative canopies have been extensively investigated (Brunet, 2020). The larger part are based on field experiments and laboratory studies, as reviewed in Raupach et al. (1996) and Finnigan (2000). Field experiments have mostly been devoted to the comprehension of exchanges of scalars between the canopy and the atmosphere above (Stoy et al., 2013) and less on how the flow interacts with the forest due to the structural limitations of field experiments. Typically, the experimental site comprises a single monitoring mast (Leuning et al., 2005; Sogachev et al., 2005) or a limited number of instrumented levels along the tower (Clausnitzer et al., 2011). Also, the comprehension of flow and turbulence within a forest canopy is driven by the upwind conditions and the single-mast experimental design does not provide sufficient information about it (Shaw et al., 1988; Su et al., 1998). The experimental limitations can be overcome by comprising numerical simulations to investigate canopy flows on the entire forest domain Gross (2012). In particular, the Reynolds-Averaged Navier–Stokes (RANS) simulation approach with the $k-\varepsilon$ turbulence closure has been adopted by Katul et al. (2004) and Dalpé and Masson (2009) among others, obtaining reliable results with a moderate computational cost. Numerical simulations of this type, which resolve the time-averaged velocity field and model all the turbulent contributions, are useful to characterise the air dynamics. They provide a clear picture of the motion and turbulent field of the entire forest and the overlying atmosphere, overcoming the spatial limitations of experimental studies (Gavrilov et al., 2011; Morales Garza et al., 2019b). The RANS simulation approach is based on relatively simple turbulence modelling; thus, an assessment of the accuracy of the results against measurements is necessary (Morales Garza et al., 2019a). More recently, emphasis has been placed on improving the accuracy of RANS simulations, e.g. through calibrated turbulence models (Lopes et al., 2016), non-homogeneity and canopy morphology (Desmond et al., 2014), and tree modelling (Kormas et al., 2016). In parallel, the Large-Eddy Simulation (LES) methodology paved the way for a more precise and direct study of turbulence from canopy flows; e.g. the work of Shaw and Schumann (1992) and Su et al. (1998) on turbulence structures above and within the forest, while Cintolesi et al. (2021b,a) investigate turbulence effects in the urban canopy. Bohrer et al. (2009) showed how a heterogeneous canopy structure affects turbulent figures, i.e. induces an increase in spatial correlation in the cycle of ejection-sweeps events and turbulent flows. Banerjee et al.

* Corresponding author.
E-mail address: francesco.barbano3@unibo.it (F. Barbano).

https://doi.org/10.1016/j.agrformet.2023.109557
Received 10 October 2022; Received in revised form 23 May 2023; Accepted 5 June 2023
Available online 21 June 2023

(2017) found that the general phenomenon of canopy convective effect (high heat flow even in the presence of low-temperature differences) is a general characteristic of canopy turbulence. Shaw and Patton (2003) analysed how wake-turbulence impacts turbulent kinetic energy (TKE) dissipation processes, transferring energy from the larger to the sub-grid scales. LES has also been applied for improving the understanding of canopy flow dynamics for multiple applications, such as particle dispersion (Pan et al., 2015) and wildland fire impact (Mueller et al., 2014). More in general, Clark et al. (2007) reported an analysis of the influence of atmospheric wind impacting the forest leading edge on the characterisation of regions of motion within the canopy. Yang et al. (2006b,a) focused on the study of turbulence statistics across the edges by characterising in detail the smooth-to-rough transition between the upwind field and the forest in terms of first- and second-order statistics. Dupont et al. (2011a) showed the main characteristics of the edge flow in a maritime pine forest, which exhibits differences from the more homogeneous forest with uniform vertical foliage distribution. Other works have studied the non-homogeneity of the forest, for example according to the plant distribution (Schlegel et al., 2012, 2015). Typically, the characterisation of in-canopy regions of motion is expressed in terms of geometric parameters, not considering the dynamic variables of the system. This raises a question as to the general validity of these results. In this context, Cassiani et al. (2008) numerically studied the canopy flow varying the leaf area index parameter and proposed an analytical model to localise the in-canopy recirculation region in dependence of the velocity and pressure at the forest edge.

Previous results established that not only the forest acts as a sink of momentum for the atmospheric wind and develops distinctive regions of motion within it, but also generates additional pressure and drag forces that modify the flow field surrounding the vegetated canopy. Following the work by Belcher et al. (2003), homogeneous canopy layers modify the incoming flow field according to the geometrical parameter of the canopy. A framework of flow modification and categorisation into regions of motion was first theorised by Belcher et al. (2008) specifically for homogeneous forests and finalised by Belcher et al. (2012), where this framework supported the flow-field description around and inside the isolated forest studied in Dupont and Brunet (2009). According to Belcher et al. (2012), six main regions of motion assemble within a homogeneous forest: (i) the impact region, upwind of the forest edge, (ii) the adjustment region, in the forest near the edge, (iii) the canopy interior region where the flow stabilises to the canopy characteristics, (iv) the canopy flow region, (v) the exit region where the flow re-adjust after the end of the forest, and (vi) the wake region where the flow recovers a logarithmic profile. Coherent structures have been detected at both edges (regions ii and v) and inner forest above and within the canopy (regions iii and iv), coupling the canopy with the atmosphere above (Eder et al., 2013). The impact region embraces the terrain-to-forest transition where a secondary circulation develops (Eder et al., 2013). In the presence of dispersion of pollutants (or other scalars), the horizontal transport exerted by mean flow and turbulence at the forest edge fosters the accumulation of contaminants downstream of the forest edge (Kanani-Sühring and Raasch, 2015). The adjustment region is a transition area where the flow adjusts to the forest structure, where a sequence of coherent structures regulates momentum and mass exchanges between the canopy and the free atmosphere (Dupont and Brunet, 2009). The magnitude of the scalar fluxes increases with a regular decrease afterward, developing non-homogeneous horizontal turbulence (Klaassen et al., 2002; Klaassen and Sogachev, 2006), while momentum fluxes are stabilised by the pressure gradient at the edge (Klaassen et al., 2002). The horizontal extension of the adjustment region can vary according to forest characteristics (vegetation density, tree species, heterogeneity) and atmospheric flow intensity, and is often determined as a function of canopy height (Morse et al., 2002). Less studied is the exit region, where an increase of the wind speed is detected together with a downward motion due to mass conservation (Belcher et al., 2003). The canopy interior region sees the decomposition of the (horizontal) velocity profile along a vertical line into two parts: an in-forest profile and an out-forest profile which follows the classical logarithm profile of the atmospheric boundary layer. The two profiles connect in an inflection point located above the canopy, showing an analogy with the plain mixing layer theory (Jimenez et al., 1985). Rannik et al. (2003) developed a piecewise analytical function describing a horizontally homogeneous and stationary flow inside and above the forest canopy. The turbulent transport between the canopy and the atmosphere above is the main driver of momentum and mass exchanges along the vertical direction, together with the turbulent structures arising inside the canopy (Poggi et al., 2004). The TKE is mostly generated by mechanical processes and the in-canopy dissipation is expressed as a function of elevation (Banerjee et al., 2018). All these features depend on foliage density to canopy top and the distance from the forest edges (Ma et al., 2020), but also the horizontal forest heterogeneity plays a critical role. For example, a low density of foliage in the undergrowth generates areas of weak recirculation within the canopy, while cavities within the canopy are known to develop recirculation zones altering both internal ventilation and turbulence structures (Banerjee et al., 2013), forcing canopy-top turbulence and skewness of the wind components (Boudreault et al., 2017). In the presence of undergrowth with little vegetation, a jet-like motion can be observed in the lower part of the forest. This starts from the upwind edge of the forest and extends to the adjustment region (Dupont et al., 2011b), triggering velocity advection that alters the intensity of the vertical fluxes and of mass exchanges (Sogachev et al., 2008). Finally, edge heterogeneity affects the impact region upwind to the forest by restructuring flow and turbulence characteristics of the coherent structures (Bailey and Stoll, 2013; Dellwik et al., 2014).

Overall, vertical and horizontal heterogeneity in the forest canopy emerged as key factors influencing the in-canopy flow and turbulence fields. A non-homogeneous forest is observed to produce specific modifications in the airflow, and it is expected to modify the regions of motion established in the Belcher et al. (2012) framework. The present study intends to build upon this existing framework and the known characteristics of forest heterogeneity to reach the following goals:

- Capture how the unperturbed flow dynamics and turbulence are modified due to the vertical heterogeneity of a real-world forest canopy;
- Expand the classification by regions of motion in a homogeneous forest, to account for vertically non-homogeneous forests;
- Introduce a quantitative parameter (the in-canopy stability parameter) for determining regions of motion within the forest that is a function of the dynamic parameters of the system.

To achieve these scopes, the experimental and simulation approaches are used together to complement each other and allow a realistic representation of the air dynamics in and around a real forest. A specially designed experimental campaign was conducted, enabling a detailed analysis of vertical transport through the canopy and, at the same time, validating a numerical simulation. The result is a global analysis of the air dynamic and turbulent features of a real forest, which combines single-point measurements with two-dimensional numerical simulations. Particularly, measurements allow a quadrant analysis to infer the turbulent momentum transport. Numerical simulations are performed using the RANS technique with the $k-\varepsilon$ turbulence model, which allows a careful inspection of the in-forest ventilation and the identification of specific dynamic regions extending and expanding Belcher et al. (2012) categorisations to include novel dynamic layers and regions of motion for vertically non-homogeneous canopies. Simulations are performed on a two-dimensional domain.

The paper is structured as follows: Section 2 reports the description of the case study and the experimental campaign; Section 3 focuses on quadrant analysis and turbulent features across the canopy; Section 4 presents the simulation model and the case setup; Section 5 shows the

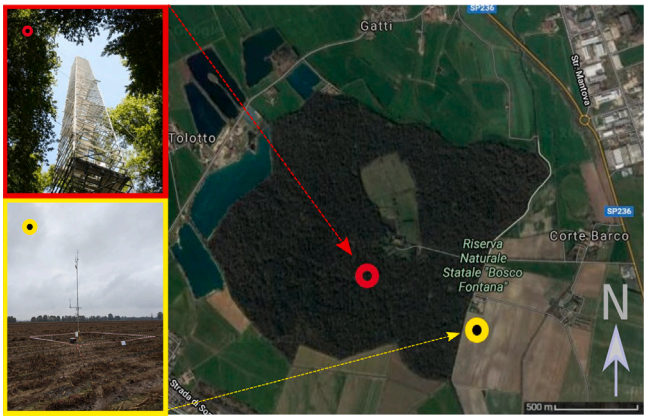

Fig. 1. Satellite view of Bosco Fontana State Nature Reserve, Str. Mantova 29, 46045 Marmirolo, Italy. Left-side photos: The forest masts (red) and the field mast (yellow). *Source:* Google Earth.

validation of the simulation with experimental data; Section 6 studies and analyses the forest ventilation through numerical simulation; Section 7 summarises the results and draws some final comments.

2. Case study and experimental campaign

An intensive field campaign was performed during autumn 2019 (26/10/2019–14/11/2019) within the forest of 'Bosco Fontana', a natural reserve located in the flat land of the Po Valley in North Italy (45°11'52.2" N, 10°44'31.2" E, 25 m a.s.l.). The forest is composed of deciduous trees of mature oaks and hornbeams covering a dense undergrowth of shrub and low-stemmed vegetation (Dalponte et al., 2008). The natural ecosystem of this forest is preserved without external human maintenance, thereby the forest debris and rotten organisms are left on the forest floor to stimulate microbial decomposition and enhance the biodiversity (Chiesa et al., 2019). The forest topography is characterised by sharp boundaries where the well-developed forest is abruptly interrupted and cultivated fields begin, see Fig. 1. Trees grow with horizontally homogeneous density on a quadratic surface of 2.35 km^2, with the exception of the historical palace and courtyard in the northern part of the forest. Tree's characteristics are homogeneous, with a nominal average height of $h \simeq 25$ m and an average Leaf Area Index (LAI) $\lambda = 3.5$ (Gerosa et al., 2017). For the campaign duration, the forest preserved the summer confirmation with full foliage thanks to the warm autumn.

2.1. Monitoring sites

The experimental field campaign aimed at characterising the dynamics and turbulence of a natural vegetation canopy. The experimental design aimed at overcoming typical limitations of field campaigns by maximising the number of sensors level within and above the forest canopy and providing a realistic upwind reference. Two monitoring sites (Fig. 1) were located inside the forest and in the neighbouring cultivated field (hereafter labelled as forest mast and field mast, respectively). The forest mast is a permanent tower of 40 m located within the forest, 750 m inwards from the south-eastern edge (Chiesa et al., 2019). It has five measuring levels z_j (with $j = 1, 2, \dots, 5$) located at: $z_1 = 4$ m ($z/h = 0.16$) in the upper part of the undergrowth, $z_2 = 8$ m ($z/h = 0.32$) and $z_3 = 16$ m ($z/h = 0.64$) at the crown heights, $z_4 = 24$ m ($z/h = 0.96$) at the forest upper edge, and $z_5 = 40$ m ($z/h = 1.6$) accessing the atmosphere above the forest. Levels z_2 and z_5 are equipped with HS-50 sonic anemometers (Gill, Lymington, Hampshire, UK) sampling at 10 Hz, while at the remaining three levels the WindMaster 3D (Gill, Lymington, Hampshire, UK) anemometers measure wind velocity and sonic temperature with a sample rate of 20 Hz. The field mast was placed on the rural field at 70 m south-east from the south-eastern forest edge, along the direction of the principal winds (see Section 3). It consisted of an antenna pole mounted on a tripod deploying two measuring levels at $z_6 = 4$ m ($z/h = 0.16$) and $z_7 = 7$ m ($z/h = 0.28$). Each level was equipped with a sonic anemometer WindMaster 3D.

The system of reference adopted is centred at the forest edge: The x-axis is the line connecting the field and forest masts while the positive direction is from east to west, which is also approximately the direction of the main wind; the y-axis roughly follows the forest edge in the direction south–north. The z-axis is the vertical direction. The velocity components are indicated both as u, v, w in the x, y, z-direction respectively, or using the repeated index notation u_i with $i = x, y, z$ when necessary for the sake of brevity.

Table 1
Selected date and time period for data analysis. Stability and wind direction are mean values, averaged over the entire time period.

Date	Time period (GMT + 01:00)	Stability $(z-d)/L_O$	Wind direction
30/10/2019	03:30–17:00	3.92×10^{-2}	E-SE

2.2. Data preprocessing

The experimental dataset went through a qualified preprocessing procedure suitable for turbulence analysis in canopy layers (Barbano et al., 2021). Data were preliminary checked to filter non-physical values by removing data that are out of the following typical ranges for the studied region: (i) sonic temperature $|T| \leq 50$ °C, and (ii) wind velocity components $|u_i| \leq 20$ m/s. Following (Vickers and Mahrt, 1997), a despiking process is performed to remove the stochastic errors resulting in sudden and isolated spikes in the time series. Specifically, values larger than 3.5 standard deviations from a moving average computed over windows of three consecutive measurements are rejected and replaced with the linear interpolation between the window values. The process is iterated until no more spikes are detected. The velocity components are rotated to align with the streamline reference system, i.e. along the mean wind direction. The entire rotation procedure is evaluated according to McMillen (1988). Throughout this paper, mean atmospheric variables $\bar{X}$ are computed using a 30-min block average of the measured ones X, and fluctuations as $X' = X - \bar{X}$.

2.3. Sub-period selected for the analysis

A time period for the analysis is selected to ensure a stationary local flow regime under neutral stability, and identified satisfying the following five conditions:

1. Wind velocity in a quasi-steady state, i.e. $\Delta u_i/\Delta t \leq 3$ m/s^2, where Δt is the time step between two consecutive 30-min averages;
2. Wind direction γ constantly from East (60°–120°) or West (240°–300°), so that the field mast is always upwind or downwind to the forest edge;
3. Clear sky conditions, i.e. no precipitation and solar radiation $I > 200$ W/m^2 at the ground;
4. Absence of synoptic forcing (from Global Forecast System synoptic maps);
5. Near-neutral stability, i.e. $|\Gamma| \leq 5\times10^{-2}$, with $\Gamma = z - d/L_O$ for the forest mast and $\Gamma = z/L_O$ for the field mast; $d = \frac{2}{3}h$ is the displacement height (Arya, 1998) and L_O the Obukhov length.

The Obukhov length is computed as $L_O = -u_*^3\theta_0/\kappa g\overline{w\}\theta'}$, where θ_0 is the potential temperature at the surface, $\kappa = 0.4$ is the von Kármán constant, g is the gravity acceleration, and $\overline{w\}\theta'}$ is the turbulent heat flux. By applying the aforementioned conditions, a single period of 13.5 h is identified, as reported in Table 1.

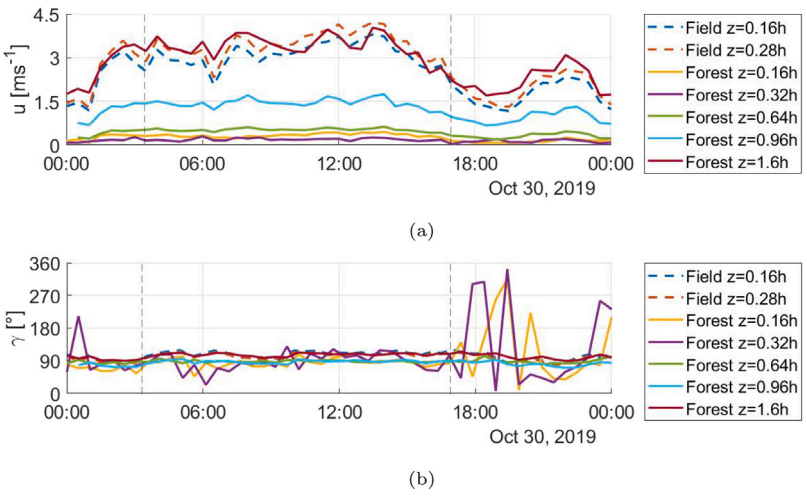

Fig. 2. The wind velocity and direction for the selected time period is reported between the vertical black dashed lines. Time series at the measuring points of the field (dashed lines, labelled as 'Field') and forest (solid lines, labelled as 'Forest') masts. Panel (a): wind velocity u; panel (b), wind direction γ.

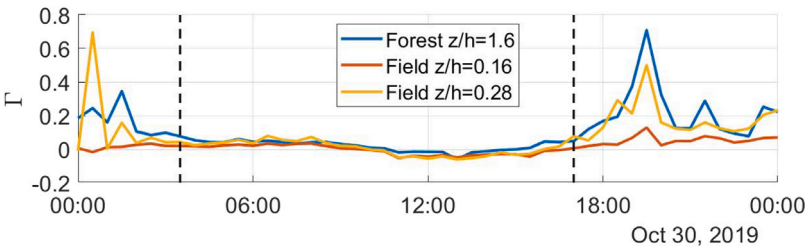

Fig. 3. Stability index Γ for the selected period enclosed between the vertical dashed black lines. At the forest mast ('Forest') $\Gamma = z - d/L_O$, while $\Gamma = z/L_O$ at the field mast ('Field').

3. Mean flow and turbulence analysis from experimental campaign

The experimental dataset has been analysed to investigate the atmospheric flow characteristics in the selected time period. Fig. 2 shows the wind velocity and direction measured at the field and forest masts. The atmospheric wind is characterised by mean easterly winds from $\gamma = 100°$; hence, the field is constantly upwind to the forest. The flow can be considered in steady-state: outside the forest, the averaged streamwise velocity u ranges between 2 and 4 m/s; within the forest, the vegetation reduces the velocity between 0 and 0.8 m/s according to the foliage density. Outside the forest, the atmospheric boundary layer is under persistent near-neutral conditions (see Fig. 3), with thermal effects becoming negligible. The inertial forces remain the only driver of the local dynamics, with the aerodynamic effects of the canopy being the major responsible for the in- and out-forest circulation.

3.1. Quadrant analysis

The dynamic interaction between the canopy and the atmosphere is analysed through the quadrant analysis. The momentum exchange induced by the turbulent kinematic momentum flux $\phi_t = u'w'$ is studied through the distribution of the velocity fluctuation components u' and w' on a Cartesian plane (scatter plot). Each quadrant of the plane identifies a specific turbulent event:

Q1 (quadrant $u' > 0$, $w' > 0$) outward interaction;

Q2 (quadrant $u' < 0$, $w' > 0$) ejection events;

Q3 (quadrant $u' < 0$, $w' < 0$) inward interaction;

Q4 (quadrant $u' > 0$, $w' < 0$) sweep events.

In the context of forest canopies, ejection (Q2) and sweep (Q4) are the most frequent and intense events (Raupach et al., 1996), and the principal contributions to the vertical transport (Gardiner, 1994; Kruijt et al., 2000). The former indicates the transport of momentum from the canopy to the free atmosphere, while the latter indicates a turbulent transport in the opposite direction. Inwards and outwards interactions describe the counter-gradient motions (with respect to the flux-gradient relationship) directed along the vertical.

The quadrant analysis is here performed at each measuring level of the forest mast, using a combination of scatter plots (addressing the quadrant distribution of the u' and w' components together with the magnitude of each couple in the quadrant) and frequency distribution per event. This investigation serves to characterise turbulence properties along the vertical, revealing how wind fluctuations are impacted by the undergrowth, trunks, foliage, and the forest drag above the canopy top. It also paves the way for further detailing of the in-canopy vertical structure obtained through numerical simulations. It is worth mentioning that the RANS approach does not allow for the instantaneous turbulence to be resolved directly, including the velocity fluctuations and the sweep and ejection events, but their contributions are accounted for in the simulated TKE, dissipation and budget terms. Both quadrant analysis and simulation add independent pieces to the description of flow and turbulence behaviours and categorise the dynamic regions of the forest.

Figs. 4b–f show the scatter plots of u' and w' at each measuring level, normalised by the standard deviation. For better visualisation, the smaller fluctuations at each level j of the mast are filtered using the hyperbolic threshold $|\phi_t^j| > K|\langle\phi_t^j\rangle|$, where $K = 4$ in agreement with commonly used values from different experiments (Nakagawa and Nezu, 1977; Antonia et al., 1981; Raupach, 1981), and the angular bracket denotes the ensemble average. The percentage of events in each quadrant is reported in Table 2. From Table 2, ejection is the

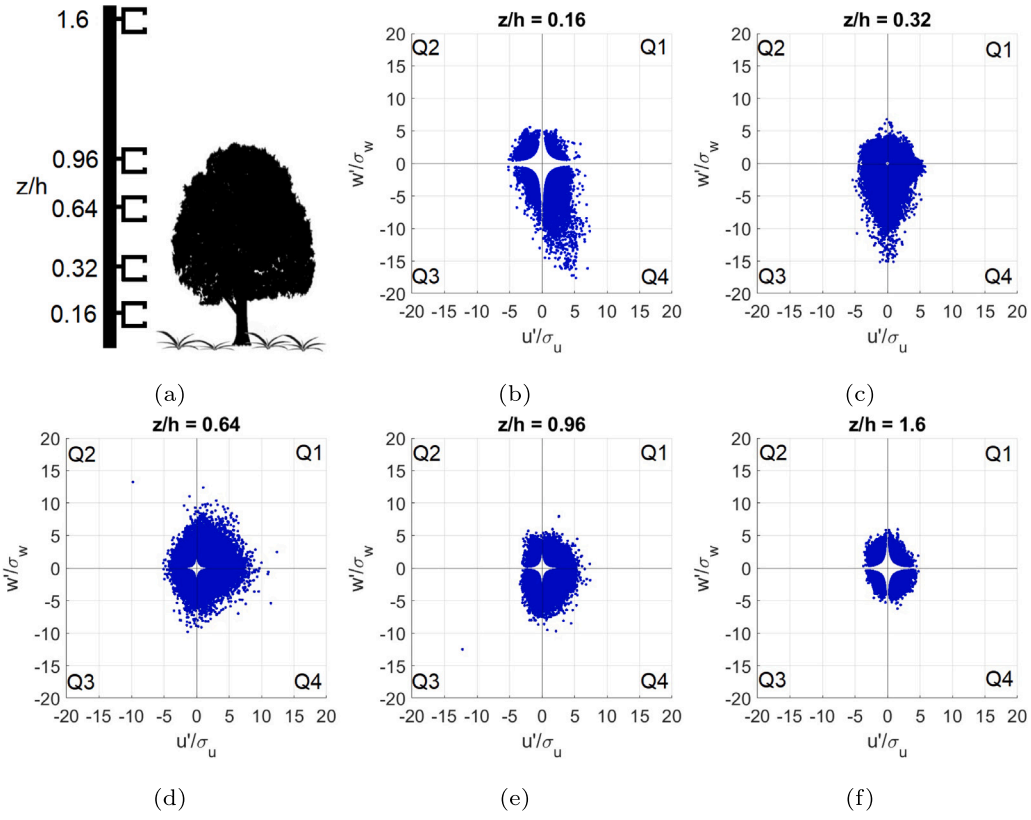

Fig. 4. Panel (a): A sketch of the measuring levels with respect to forest tree height. Panels (b-f): Scatter plots of u' vs w' for each measuring point and made non-dimensional by the standard deviations σ_u and σ_w.

Table 2
Number of events in each quadrant (percentage to the total number of events per measuring point).

Measuring levels $[z/h]$	Outward [%]	Ejection [%]	Inward [%]	Sweep [%]
0.16	17	40	12	31
0.32	24	30	24	22
0.64	20	26	32	22
0.96	20	36	23	21
1.60	21	32	23	24

most frequently observed event. However, scatter plots in Fig. 4 rarely depict ejection among the most intense events. Thus, the momentum transport associated with ejection is typically weaker than sweep, making air recirculation and trapping more efficient than fresh-air entrainment, especially within the canopy. This is observed at $z/h = 0.16$ (Fig. 4(c)), intense sweep events foster a momentum trapping within the forest undergrowth. This feature can be associated with the presence of von Kármán vortexes arising in the vicinity of the canopy ground surface, which typically displays energetic downward turbulent momentum fluxes (Poggi et al., 2004; Launiainen et al., 2007). At $z/h = 0.32$ and $z/h = 0.64$, the distribution shifts towards outwards-inwards events (Q1 and Q3), whose frequencies (see Table 2) and intensities (see Fig. 4c, d) increase as the dragging effects of the tree foliage enhance the turbulence isotropy (Belcher et al., 2012; Dupont et al., 2012) and dissipation (Yue et al., 2007). The shift between $z/h = 0.16$ and $z/h = 0.64$ marks the transition between two sublayers within the canopy where the different foliage density drives the flow and turbulence behaviours. This sublayer separation will be highlighted also by the results of the numerical simulations, suggesting the presence of two different dynamic regions within the canopy. At $z/h = 0.96$ and $z/h = 1.60$, the intensity of the momentum transport decreases and the distributions show a gentle elongation towards Q4 (Fig. 4e–f), while ejection becomes the most frequent event once again (see Table 2). The combination of a more intense sweep and frequent ejection drives a sweep-ejection regime at the top and above the canopy, causing an overall downward flux of momentum due to flow intrusion from above the forest or the presence of a recirculation zone at the canopy top.

The slow transition from nearly-isotropic fluxes to sweep-ejection regimes between $z/h = 0.64$ and $z/h = 1.60$ is also observed by Kruijt et al. (2000) under neutral atmospheric stability. Above the canopy top, $z/h \geq 1$ the sweep-ejection balance is confirmed by Gavrilov et al. (2011). In partial disagreement with our results, Gardiner (1994) observed a balance between sweep and ejection at $z/h = 1$ and a marked predominance of sweeps at $z/h = 0.75$. This difference can be ascribed to the different drag exerted by the vegetation. Gardiner (1994) investigated a forest with a characteristic Leaf Area Density (LAD) profile that tends to zero in the upper canopy, while our forest has a large LAD up to the canopy top. This morphology causes a stronger energy dissipation, favouring isotropy until the canopy top.

To quantify the relative intensity of ejection over sweep, the synthetic index $Q2/Q4$ is computed as the ratio between the average value of ϕ_t in Q2 and that in Q4:

$$\frac{Q2}{Q4} = \frac{\langle \phi_t \rangle_{Q_2}}{\langle \phi_t \rangle_{Q_4}}, \tag{1}$$

where $\langle \cdot \rangle_{Q_x}$ denotes the average of all the events located in quadrant Q_x. Fig. 5 compares the vertical profile of $Q2/Q4$ for the present case study (BF) with some from the literature, namely: Raupach et al. (1986) (R86, wind tunnel experiments in neutral conditions), Baldocchi and Hutchinson (1987) (BH87, field experiments within a neutrally stratified almond orchard), Christen and Vogt (2004) (CV04, experimental measurements in variable stability conditions). Overall, the profiles show similar features: Sweep is predominant near the ground ($z/h < 0.1$), while an increase in ejection intensity is detected in the range $0.1 \leq z/h \geq 0.3$, where the trunks are mainly free from foliage. Sweep

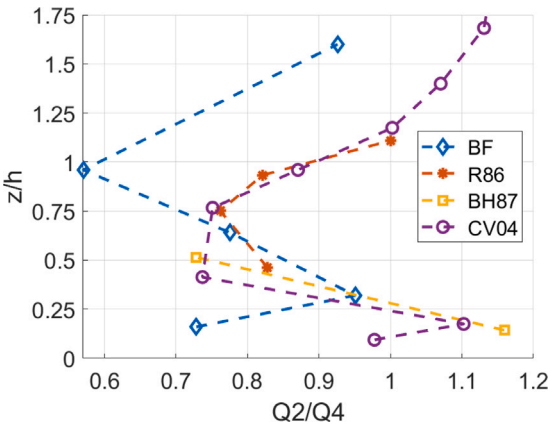

Fig. 5. Vertical profile of $Q2/Q4$ through a forest canopy of height h. Legend: BF, the present case study of 'Bosco Fontana'; R86, Raupach et al. (1986); B87, Baldocchi and Hutchinson (1987); CV04, Christen and Vogt (2004).

is one again predominant where the leaf density of the forest becomes denser ($0.32 < z/h \leq 1$), whilst ejection increases at $z/h > 1$ above the canopy top.

It is worth noting that in the present case study ejection intensity never exceeds sweep. Within the canopy ($z/h < 1$), this can be ascribed to the different planar and frontal densities of the forest: both (Baldocchi and Hutchinson, 1987) and Christen and Vogt (2004) studied forests with coarser tree density, while (Raupach et al., 1986) performed wind-tunnel experiments where aluminum strips do not fully reproduce the morphology of the real trees in terms of trunks and foliage. Above the canopy ($z/h > 1$), the roughness sub-layer (RSL) modifies the ejection-sweep balance with respect to the inertial sub-layer (ISL) above it (Finnigan et al., 2009). Within the ISL, the large eddies scale directly with the boundary-layer flow, and weak ejection conditions dominate turbulent transport ($Q2/Q4 > 1$). Conversely, the RSL is organised in coherent structures mostly caused by inflection-point instabilities and intense sweep events that drive turbulent transport ($Q2/Q4 < 1$) (Raupach et al., 1996). Numerical simulations will confirm the measurement level $z/h = 1.6$ is located within the RSL.

4. Numerical simulation approach

The analysis of the experimental dataset leads to the following modelling assumptions for the case under consideration: (i) thermal stratification does not significantly affect the overall fluid dynamics in the selected study period; thus the temperature field is not resolved; (ii) the atmospheric wind is an incompressible flow and the Coriolis force is negligible; (iii) the atmospheric flow is regular enough to be considered at a statistically steady state. Under these assumptions, the simulation technique adopted is the Reynolds-Averaged Navier–Stokes (RANS) methodology provided with a $k-\varepsilon$ turbulence model. The forest is modelled as a two-dimensional porous medium, homogeneously dense in the horizontal directions. For the sake of conciseness Einstein's notation is used in the numerical model equations.

4.1. Mathematical model

The two-dimensional RANS equations for an incompressible flow are:

$$\frac{\partial u_i}{\partial x_i} = 0 \tag{2}$$

$$u_j \frac{\partial u_i}{\partial x_j} = -\frac{1}{\rho}\frac{\partial p}{\partial x_i} + \nu \frac{\partial^2 u_i}{\partial x_j \partial x_j} - \frac{\partial}{\partial x_j}\tau_{ij} + S_{u,i} \tag{3}$$

where u_i are the time-averaged velocity components ($i = x, z$), ρ is the constant air density, p is the pressure, $\nu = 1.5 \times 10^{-5}$ is the molecular dynamic viscosity of air, τ_{ij} is the anisotropic part of the Reynolds stress tensor ($j = x, z$), and $S_{u,i}$ is the sink term that accounts for the momentum loss due to the presence of the forest. This term is set to zero outside the forest, while in the forest area it reads

$$S_{u,i} = -C_D \alpha |u| u_i, \tag{4}$$

where C_D is the forest drag coefficient, α is the LAD. The drag coefficient is linked to the ability of the forest to absorb momentum, while the LAD changes with height and depends on the forest type, i.e., the volume of leaf, trunks, and branches in a cubic meter (Lalic and Mihailovic, 2004). A sensitivity study is presented in Section 4.4 to identify the optimal LAD profile for the present case.

Table 3
Values of the $k-\varepsilon$ model constants used in the present study as adopted from Garratt (1994), Sanz (2003), and Katul et al. (2004).

C_μ	$C_{\varepsilon 1}$	$C_{\varepsilon 2}$	σ_k	σ_ε	$C_{\varepsilon 4}$	$C_{\varepsilon 5}$	β_p	β_d
0.03	1.44	1.92	1.0	2.12	0.78	0.78	1.0	5.03

4.2. Turbulence model

The RANS equations are closed using the classical $k-\varepsilon$ model proposed by Launder and Spalding (1974), as it is implemented in OpenFOAM version 6.0 (2019). Such a model has led to good results in simulating the turbulence within and above canopies (Katul et al., 2004; Svensson and Häggkvist, 1990). The anisotropic Reynolds stress tensor is modelled with the eddy-viscosity hypothesis:

$$\tau_{ij} = 2\nu_t S_{ij}, \tag{5}$$

where ν_t is the turbulent viscosity, $S_{ij} = 0.5\left(\partial u_i/\partial x_j + \partial u_j/\partial x_i\right)$ is the strain rate tensor, k is the TKE . The turbulent viscosity reads $\nu_t = C_\mu k^2/\varepsilon$, where ε is the TKE dissipation rate and C_μ (see Table 3) is computed as follows Garratt (1994):

$$C_\mu = \frac{1}{(0.5[(\sigma_{u_x}/u_*)^2 + (\sigma_{u_y}/u_*)^2 + (\sigma_{u_z}/u_*)^2])^2} \tag{6}$$

where σ_{u_x,u_y,u_z} are the standard deviations for the wind components and u_* is the friction velocity in the surface layer. Both k and ε are determined as solutions of prognostic equations which include the canopy effects on the production and dissipation of TKE:

$$\frac{\partial u_i k}{\partial x_i} = \frac{\partial}{\partial x_j}\left[\left(\nu + \frac{\nu_t}{\sigma_k}\right)\frac{\partial k}{\partial x_j}\right] + P_k - \varepsilon + S_k \tag{7}$$

$$\frac{\partial u_i \varepsilon}{\partial x_i} = \frac{\partial}{\partial x_j}\left[\left(\nu + \frac{\nu_t}{\sigma_\varepsilon}\right)\frac{\partial \varepsilon}{\partial x_j}\right] + C_{\varepsilon 1}\frac{\varepsilon}{k}P_k - C_{\varepsilon 2}\frac{\varepsilon^2}{k} + S_\varepsilon \tag{8}$$

where the production of TKE is expressed as $P_k = 2\nu_t S_{ij}\partial u_i/\partial x_j$, while S_k and S_ε account for turbulence generation due to breakage of the mean-flow motion by the canopy roughness elements. These terms are zero outside the forest domain and read:

$$S_k = \alpha C_D(\beta_p |u|^3 - \beta_d k|u|) \tag{9}$$

$$S_\varepsilon = \alpha C_D \frac{\varepsilon}{k}(C_{\varepsilon 4}\beta_p |u|^3 - C_{\varepsilon 5}\beta_d k|u|) \tag{10}$$

where β_p, β_d, $C_{\varepsilon 4}$ and $C_{\varepsilon 5}$ are model constants whose values are reported in Table 3. The quantity $\beta_p u^3$ represents the fraction of mean flow kinetic energy converted to wake-generated TKE by canopy drag (a TKE source), while $\beta_d ku$ is the fraction of TKE dissipated by the short-circuiting effect (a TKE sink) (Katul et al., 2004).

4.3. Computational domain and boundary conditions

The simulation domain is depicted in Fig. 6. The domain consists of a two-dimensional rectangular area, cutting the forest along the east–west direction passing through the field and forest masts (x-direction), with a horizontal extension of $L = 4000$ m and a vertical extension

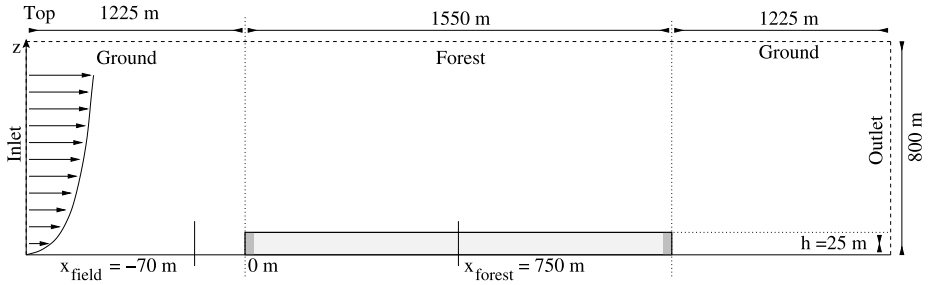

Fig. 6. Sketch of the two-dimensional geometry and dimensions of the case domain (not in scale for a clearer visualisation).

Table 4
Summary of the boundary conditions imposed following the nomenclature used in OpenFOAM version 6.0 (2019) (see the relative documentation for further details).

	Inlet	Ground	Top	Outlet
U	`atmBoundaryLayerInletVelocity`	`noSlip`	`slip`	`inletOutlet`
k	`atmBoundaryLayerInlet`	`KqRWallFunction`	`slip`	`inletOutlet`
ϵ	`atmBoundaryLayerInletEpsilon`	`epsilonWallFunction`	`slip`	`inletOutlet`
p	`slip`	`slip`	`slip`	`fixedValue`
ν_t	`slip`	`nutkAtmRough-WallFunction`	`slip`	`slip`

(z-direction) equal to $H = 800$ m. The origin of the system of reference is located in the left bottom corner of the forest outline. The forest is modelled as a rectangular porous medium with a total length of 1550 m and height $h = 25$ m. The tower mast used to collect the experimental data is located at $x_{\text{forest}} = 750$ m, while the field mast is located at $x_{\text{field}} = -70$ m.

The computational grid is composed of 420 × 102 cells in x- and z-direction, respectively. According to Dalpé and Masson (2009), the grid is stretched near the ground boundary ($z = 0$) to obtain a cell height of $\Delta z \sim 0.2$ m, and at the forest edge ($x = 0$ m) to have a computational cell width of $\Delta x \sim 2.5$ m. Vertical and horizontal stretching is obtained by a uniform expansion of the cells in such a way that the cell on the ground and on the forest edge have the desired size.

Boundary conditions are summarised in Table 4, following the nomenclature used in OpenFOAM version 6.0 (2019). The inlet ($x = -1250$ m) profiles have been modelled following Richards and Hoxey (1993) and subsequent modification by Yang et al. (2009); they are:

$$u(z) = \frac{u_*}{\kappa} \ln\left(\frac{z - d + z_0}{z_0}\right) \tag{11}$$

$$k(z) = \frac{{u_*}^2}{\sqrt{C_\mu}} \sqrt{C_1 \ln\left(\frac{z - d + z_0}{z_0}\right) + C_2} \tag{12}$$

$$\varepsilon(z) = \frac{{u_*}^3}{\kappa(z - d + z_0)} \sqrt{C_1 \ln\left(\frac{z - d + z_0}{z_0}\right) + C_2} \tag{13}$$

where $u_* = \kappa\, u_{\text{ref}} / \ln[(z_{\text{ref}} + z_0)/z_0]$ is the estimated friction velocity, $d = 0$ m is the displacement height, and the model contents are $C_1 = 0$ and $C_2 = 1$. In order to reproduce the inflow measured in the experiment for the near-neutral case, the roughness length outside the forest is set to $z_0 = 0.1$ m, while the reference values of the variables are set as follows: $u_{\text{ref}} = 8$ m/s, $z_{\text{ref}} = 800$ m, $k_{\text{ref}} = 0.26$ m^2/s^2, and $\epsilon_{\text{ref}} = 6.7 \times 10^{-5}$ m^2/s^3. Pressure and turbulent viscosity enforce a zero-gradient condition at all the boundaries. At the ground ($z = 0$), a non-slip condition is imposed for the velocity ($u = 0$) and the zero-normal gradient condition is imposed for pressure ($\partial p/\partial z = 0$), while wall functions are imposed on other variables to model the wall-boundary layer which is not directly resolved. Such wall functions are reported in Table 4 and details on the implementations can be found in the official documentation of OpenFOAM version 6.0 (2019). At the top boundary $z = 800$ m, a free interface is simulated by imposing a zero-gradient condition for all variables. At the outlet ($x = 42\,775$ m), a free stream condition is imposed for u, k and ϵ. Constant value is imposed to pressure ($p = 0$) and zero-gradient to turbulent viscosity.

4.4. Forest model and leaf-area density tuning

The forest is modelled as a vertically non-homogeneous porous medium as in Dalpé and Masson (2009). Within the forest domain, the drag force of the canopy varies with height in accordance with the LAD profile. At the forest edges, two sponge regions of width h are inserted (0 m< x < 25 m and 1525 m< x <1550) to mimic an area where vegetation grows homogeneous along the vertical, showing no discontinuity with the undergrowth. The forest drag coefficient is set to $C_D = 0.2$, the roughness length above the forest is $z_0 = 2.5$ m, and LAI is $\lambda = 3.5$ according to Gerosa et al. (2017). A sensitivity analysis is carried out to calibrate the LAD profile with the experimental measurements. This becomes necessary as conventional methods for measuring LAD were not available or feasible for this case study. Direct methods require specific instrumentation not available for this case study and a destructive, time-consuming procedure that ultimately gives the LAD for a single tree species with a known health state and age. Even considering adopting this method, a multitude of sampling should have been done covering the extension of the forest and accounting for its horizontal heterogeneity, which is unfeasible considering the forest dimension and accessibility. Various indirect methods are known from the literature, but their performance is still under debate (Jonckheere et al., 2004; Yan et al., 2019; Wei et al., 2020). For these reasons, the LAD computation is here based on a sensitivity analysis. A selection of several LAD profiles is presented together with the simulated velocity profiles compared to the experimental measurements at a vertical line corresponding to the location of the forest mast.

Fig. 7 shows five simplified LAD profiles chosen following the work of Dalpé and Masson (2009), along with the resulting mean velocity profiles. Fig. 7(a) reports three configurations: LAD11 has a constant value and represents a vertically homogeneous forest; LAD12 is constant and goes to zero at the surface; LAD13 is constant and is zero for $z/h < 0.1$ and models a forest with low and clean undergrowth. The simulated mean wind velocities are practically the same and lead to an almost zero velocity within the canopy, whilst the velocity above the canopy is in agreement with experimental data. The reduction of LAD near the ground does not affect significantly the simulated velocity, except for LAD13 where local non-zero velocity is detectable near the surface due to drag reduction. Fig. 7(b) displays two profiles modelling a vertically non-homogeneous foliage distribution with a single peak in the forest upper part $z/h = 0.8$ (LAD14) and central part $z/h = 0.5$ (LAD15). Both reproduce an almost zero velocity in the

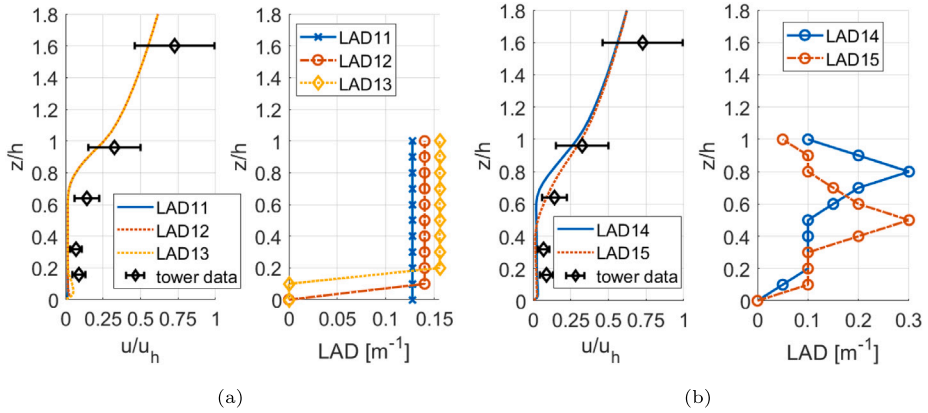

Fig. 7. Velocity profiles along a vertical line at the forest mast from the present experimental campaign (black diamonds) and from RANS simulations (coloured lines) obtained from simplified LAD profiles: (a) LAD profiles reproducing homogeneous foliage distributions; (b) LAD profiles reproducing a single-peak distribution of the foliage.

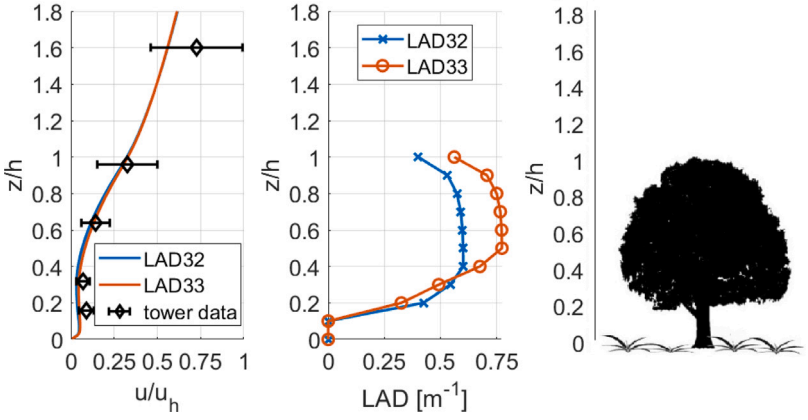

Fig. 8. Velocity profiles along a vertical line at the forest mast from the present experimental campaign (black diamonds) and from RANS simulations (coloured lines) obtained from the empirical LAD profiles proposed by Lalic and Mihailovic (2004). Sketch of a typical canopy tree with vertically non-homogeneous foliage distribution in height.

lower part of the forest ($z/h < 0.5$) and velocity values comparable with the experiment above the forest ($z/h > 1$). Differences arise at the intermediate level $0.5 < z/h < 1$, where the LAD14 underestimates the velocity as a result of a larger drag in that area. Overall, the simplified LAD profiles lead to an inaccurate reproduction of the wind velocity within the forest, which leads to an unrealistic drag distribution.

In order to better capture the wind profile within the forest ($z/h < 1$), a realistic LAD profile is required. Following the work of Lalic and Mihailovic (2004), the following empirical formula has been used to determine a set of profiles:

$$\alpha(z) = \alpha_m \left(\frac{h - z_m}{h - z}\right)^n \exp\left[n\left(1 - \frac{h - z_m}{h - z}\right)\right] \tag{14}$$

where $\alpha(z)$ is the LAD profile and α_m is the maximum value of LAD which is reached at height z_m. The exponent n is defined in two ranges: $n = n_A$ in $0 \leq z < z_m$, and $n = n_B$ in $z_m \leq z \leq h$. The parameter α_m can be estimated from the characteristics of the forest's trees, but also imposing the integral of Eq. (14) to be equal to the LAI. Instead of resolving numerically such an integral, we applied the integral mean value theorem to obtain a simplified expression: $\alpha_m = C_\alpha(\lambda/h)$, where C_α is an additional model constant. The optimisation of the LAD is made by tuning n_A, n_B, z_m, and C_α on the measured velocity profile. Fig. 8 presents the result of this optimisation: LAD32 (where $n_A = 12$, $n_B = 0.1$, $z_m = 0.5h$, and $C_\alpha = 5.3$), and LAD33 (where $n_A = 12$, $n_B = 0.1$, $z_m = 0.4h$, and $C_\alpha = 4.3$). Both profiles lead to a satisfactory reproduction of the velocity intensity within and above the forest. A negligible difference is detectable in the range $0.4 < z/h < 0.7$, where the LAD32 produces slightly lower velocities due to the lower value of z_m. It is found that z_m is the parameter that mainly affects the resulting velocity profiles, while the sensitivity to the variation of other parameters is generally lower.

The agreement between simulated and measured wind profile provides an indirect evaluation of the LAD32 and LAD33 consistency with the studied forest; therefore, the profile LAD33 is adopted for the numerical simulations. Such a profile accounts for a sparse undergrowth ($z/h < 0.1$), and trees with a vertically non-homogeneous foliage distribution where the foliage density smoothly increases with height within the interval $0.1 < z/h < 0.5$ and slightly decrease in the upper part ($0.9 < z/h < 1.0$) of the canopy.

4.5. Non-dimensional numbers

Different definitions are possible for the Reynolds number of an atmospheric flow through a forest. Following Gromke (2018), the Reynolds number based on the forest height is defined as $Re_h = hu_h/\nu$, with u_h being the unperturbed atmospheric velocity at the forest top. Such parameters can be computed from the velocity boundary condition by utilising the logarithmic boundary-layer law to project the velocity at height h. The case study numerically reproduced is characterised by an average velocity at the forest top $u_h = 5$ m/s evaluated from the velocity profile at the inlet, which leads to a Reynolds number of $Re_h = 8.3 \times 10^6$. Other possibilities for the reference velocity include computing u at the top of the numerical domain. Although reasonable, this choice depends on the domain size which is arbitrarily defined by the user. Using u_h is here preferred since h is a representative non-arbitrary height in the domain, only dependent on the geometry of the canopy.

In the case of a vertically homogeneous canopy, i.e. constant LAD along z-direction, additional parameters appear when momentum equations (3) are made non-dimensional by means of the forest height h and the characteristic velocity u_h. Such parameter is named the canopy drag number and reads:

$$N_c = \frac{h}{L_c}, \tag{15}$$

where $L_c = \alpha C_D$ is the canopy drag length. The N_c depends only on the canopy structure and is directly proportional to the momentum sink exerted by the canopy. For a vertically non-homogeneous canopy, a bulk canopy drag number using $\lambda \sim h\langle\alpha\rangle_z$, where $\langle\alpha\rangle_z$ is the LAD averaged along the vertical direction. Hence, the canopy drag length reads $L_c = h/\lambda C_D$. In the present case, $L_c = 36$ m and $N_c = 0.7$. It is worth noticing that L_c can be used as an alternative length scale for the dynamic system instead of h when the drag effects are predominant.

4.6. Numerical settings

The numerical model is implemented in OpenFOAM version 6.0 (2019), an object-oriented toolbox for fluid dynamics, written in C++. The software is open-source and uses the finite volume method. Simulations have been carried out using the `simpleFoam` solver, while the porous source terms of Eqs. (4), (9) and (10) have been implemented following the documentation by Segersson (2017). The second-order scheme is used for all spatial derivatives, except for the non-linear terms which are discretised by the `bounded Gauss limitedLinear 1` scheme, that is second-order accurate switching to first order to stabilise the computation in regions of rapidly changing gradient. The threshold for residuals is $r_{tol} = 10^{-4}$ for all quantities.

5. Validation of the simulation approach

The simulation approach is validated against the experimental dataset of the measuring campaign and analytical expressions. Prior to the validation, a mesh sensitivity study has been performed: The number of cells of the actual computational grid was increased and decreased by 25% and 50% in all directions. The results show that velocity and TKE profiles along selected vertical lines collapse on the same curves when the grid is varied by 25%, while results deteriorate when the grid points are reduced by 50%. Hence, the present simulation results are not grid-dependent.

Numerical and experimental profiles are compared with the analytic functions from Rannik et al. (2003). In this work, the streamwise velocity profile is described by a piecewise function, which is defined into three sub-domains of the boundary layer in the vertical direction: The canopy sub-layer (CSL) located within the forest canopy, $0 \le z < h$; the RSL above the canopy, $h \le z < Z_*$, the ISL above the forest, $Z_* \le z$ (Belcher et al., 2012). The analytical velocity profile reads as follows:

$$u_{abl}(z) = \frac{u_*}{\kappa}\left[\ln\left(\frac{z-d}{z_0}\right) - \psi_m\left(\frac{z-d}{L_O}\right) + \psi_m\left(\frac{z_0}{L_O}\right)\right] \quad \text{if } Z_* \le z \tag{16}$$

$$u_{rsl}(z) = u_{atm} + \frac{u_*}{\kappa}\int_z^{Z_*} \psi_m\left(\frac{z-d}{L_O}\right)\frac{1-\gamma_m(z)}{z-d}dz \quad \text{if } h \le z < Z_* \tag{17}$$

$$u_{csl}(z) = u_h \exp\left[\alpha_u(z/h-1)\right] \quad \text{if } 0 \le z < h \tag{18}$$

where the stability function $\psi_m = -6(z-d)/L_O$ depends on the Obukhov length and the canopy attenuation coefficient is estimated to $\alpha_u = 2$ through exponential fitting. The function γ_m accounts for roughness sub-layer effects and reads as

$$\gamma_m(z) = \left(\frac{z-d}{Z_*-d}\right)^{\eta}, \tag{19}$$

where the coefficient $\eta = 0.6$ is set according to Rannik et al. (2003). The roughness length is set to $z_0 = 0.1$ m and the roughness sub-layer depth is set to $Z_* = 2h$ according to previous studies (Flerchinger et al., 2015; Harman and Finnigan, 2007).

The theoretical profile of TKE is evaluated as follows: Above the forest ($z \ge h$), it takes a constant value $k_a = 1.7\,\mathrm{m}^2/\mathrm{s}^2$ which is the TKE at $z/h = 1.6$ averaged over the analysed period, while inside the forest ($z < h$), it reads

$$k = \frac{1}{2}k_a(\sigma_u^2 + \sigma_w^2) \tag{20}$$

where

$$\sigma_i = \left[(1-\gamma_i)e^{-\alpha_i(1-\frac{z}{h})^{\beta_i}} + \gamma_i\right] \tag{21}$$

with $i = (u, w)$, $\alpha_i = (1, 0.9)$, $\gamma_i = (-0.3, -0.63)$ following Rannik et al. (2003).

Fig. 9(a) shows the non-dimensional streamwise velocities at a vertical line coincident with the forest mast. Overall, the simulated velocity profile inside the canopy ($0 < z/h < 1$) accurately reproduces the experimental data, as expected after the tuning of the LAD profile. It is worth noting that in the lower forest ($z/h < 0.25$), the simulations reproduce a local maximum as a consequence of the reduced LAD near the ground (Fig. 8). Above the canopy ($z/h > 1$) the simulation slightly underestimates the wind velocity but remains within the experimental uncertainty. Near the canopy boundary ($z/h = 1$), the velocity displays an inflection point and a change of concavity. This is a typical effect of the in-canopy drag and the wind profile adjusts to the larger-scale flow taking the characteristic logarithmic shape. This inflection point has been mostly observed within layers of strong wind shear at the canopy top (e.g., Raupach et al. 1986, Poggi et al. 2004). The piecewise theoretical profiles (composed of RSL and CSL in Fig. 9) are in reasonable agreement with experimental data and simulations. Nonetheless, a few discrepancies are evident, especially inside the canopy. Specifically, the decrease of the velocity intensity in the central region of the forest ($0.25 < z/h < 0.75$) is not predicted by the theoretical exponential law of Rannik et al. (2003), while the velocity increase at the canopy top and bottom is underestimated or even not accounted for. The analytical functions were developed for a homogeneous forest and therefore not taking into account the different leaf distributions given by the LAD profile. Note that this shortcoming does not compromise the ability of the analytical function to capture the overall in-canyon velocity; the location of the mast within the inner region of the forest is such that the flow penetration in the trunk area is already reduced to a value much closer to that in the foliage area. In the inner region only, the analytical solution becomes a reasonable approximation. Above the canopy ($z/h > 1$) the profile underestimates both the simulation and the experimental data.

Fig. 9(b) reports the non-dimensional TKE at the same vertical line as Fig. 9(a). Measurements show that in the lower ($z/h < 0.25$) and central ($0.25 < z/h < 0.75$) parts of the forest, the TKE has very low values due to the drag generated by the trees. In the upper part ($0.75 < z/h < 1$), the interaction with the atmospheric wind rapidly increases the TKE and, hence, the turbulent content of the flow. This is due to the large wind shear production of TKE also reported by Kaimal and Finnigan (1994). Above the canopy ($z/h > 1$) TKE level stabilises to a constant value. Globally, simulation results are in satisfactory agreement with experimental profiles but slightly underestimate the TKE near the ground and above the canopy. On the contrary, the theoretical profile tends to predict higher TKE values within the canopy.

Fig. 10 shows the non-dimensional streamwise velocities and TKE at the vertical line coincident with the field mast. The simulated streamwise velocity is in good agreement with the experimental data (Fig. 10(a)), and it is also consistent with the theoretical log-linear profile passing through the $z/h = 0.28$ measuring level. The theoretical TKE profile in Fig. 10(b) is obtained through exponential fitting of the empirical function $z/h = a\exp(-bk)$ (Shi and Yeo, 2016) on our data, obtaining $a = 1.2 \times 10^4$ and $b = 8.14$. The simulation is not able to reproduce the TKE profile at the field mast. This is an effect of the simplified boundary condition for TKE imposed at the inlet. Such an inlet profile rapidly adjusts to a more realistic profile in the presence of

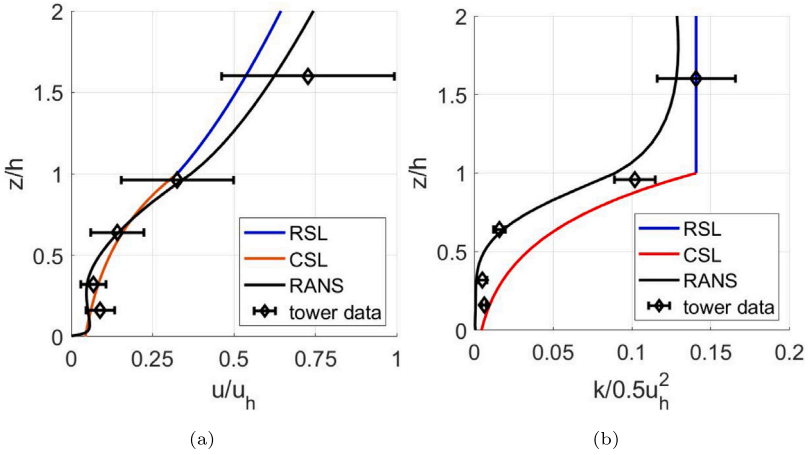

Fig. 9. Non-dimensional mean streamwise velocity and TKE at a vertical line corresponding to the location of the tower mast. Black solid line, RANS simulation results; blue solid line, theoretical profile in the sub-layer (RSL); red solid line, theoretical profile inside the canopy (CSL); black diamond, experimental measurements from field campaign (tower data). Streamwise velocities and TKEs are made non-dimensional using the streamwise velocity at the canopy top.

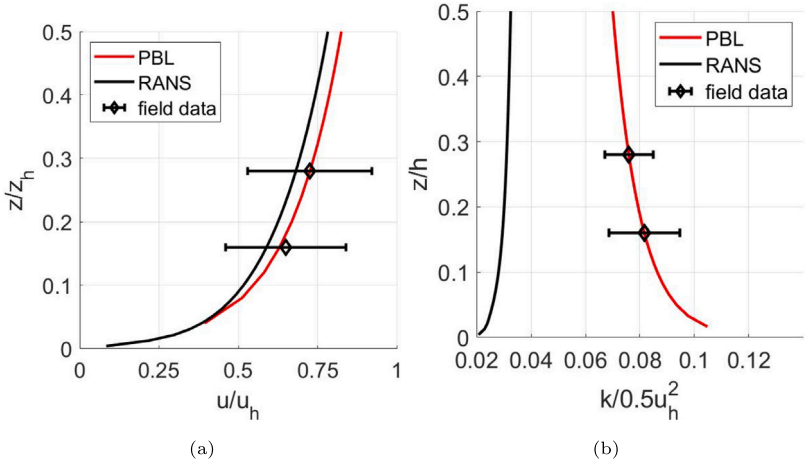

Fig. 10. Non-dimensional mean streamwise velocity and TKE at a vertical line corresponding to the location of the field mast. Black solid line, RANS simulation results; red solid line, theoretical profile on flat terrain (PBL); black diamond, experimental measurements from field campaign (field data). Streamwise velocities and TKEs are made non-dimensional using the streamwise velocity at the canopy top.

obstacles or complex geometries (e.g., the TKE profile above the forest is in agreement with the measured data), but in the case of smooth and flat terrain persists in space. This is a known shortcoming of the numerical model adopted. It is indeed required to impose a simplified TKE profile at the inlet, which stabilises the simulation but persists with minimal variations in the field region while immediately adjusting to a realistic profile in the forest region. Notice that such feature does not affect the overall accuracy of the simulation in the forest region, as already observed in Fig. 9(b). Hence, the simulation results are considered reliable in the forest area that is the focus of this study; whilst in the field region ($x < 0$) the velocity field is realistic but the TKE is not.

Overall, the simulation methodology and settings provide results in satisfactory agreement with the experimental data and the theoretical results reported in the literature. Hence, the simulation is considered successfully validated and is used to analyse the velocity field in the whole forest domain.

6. Forest flow analysis through numerical simulations

The numerical simulations are utilised to analyse the overall dynamics within and above a single finite and vertically non-homogeneous canopy.

6.1. Flow around the forest and characterisation of the roughness sub-layer

The overall flow around the forest is described by the distribution of mean and turbulent quantities in a vertical plane around the forest. Quantities are made non-dimensional by forest height h and the approaching flow velocity u_h at the forest top.

Fig. 11 shows the spatial distribution of non-dimensional velocity components, pressure, and TKE around the forest (with extension $0 < x/h < 62$), in a rectangular region $0 < z/h < 10$ and $-10 < x/h < 72$. When the atmospheric wind approaches the forest upwind edge ($x/h = 0$), the flow penetrates the forest as it deviates upwards: Streamwise velocity is reduced by the canopy drag, while a peak of positive vertical velocity drives the flow above the upwind edge. A strong horizontal pressure gradient is detectable since the forest acts as an obstacle to the atmospheric wind. Far from the edges, the pressure gradient and vertical velocity practically vanish, and the streamwise velocity is reduced within the forest by the canopy drag. Near the downwind edge ($x/h = 62$), negative vertical and horizontal pressure gradients develop: The former deflects velocity downwards at the downwind edge of the forest, and the latter helps the flow to exit from the forest (Li et al., 1990). The TKE is generated at the interface between the forest top boundary and the surrounding flow: A zone of high turbulence intensity is located above and downstream the forest upwind edge, it is transported in the vertical direction in the central part of the forest

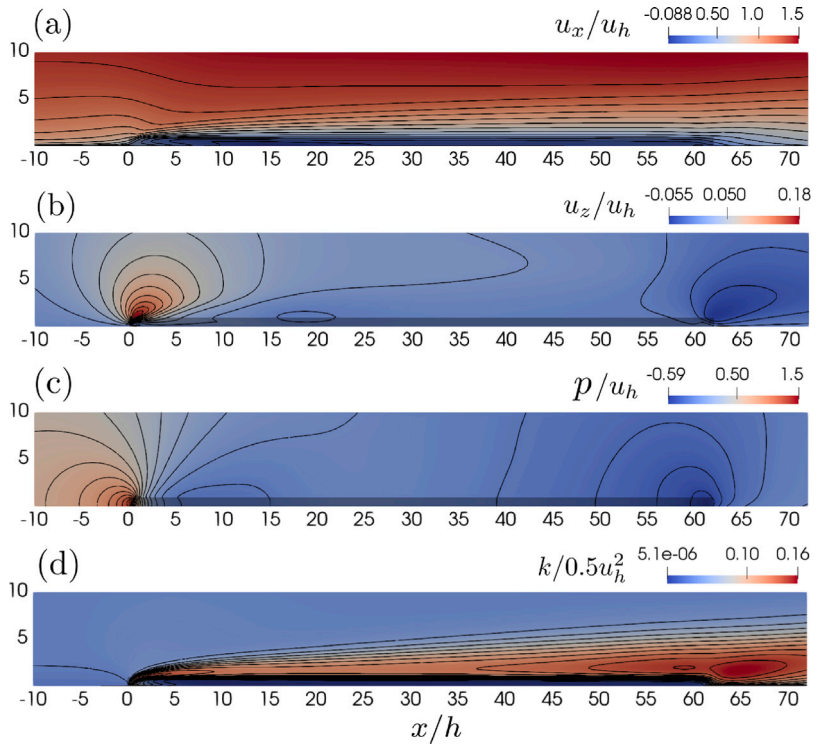

Fig. 11. Spatial distribution of non-dimensional variables in the forest region: (a) streamwise velocity; (b) vertical velocity; (c) pressure; (d) TKE. For each variable, 15 contour lines are drawn. The black rectangle represents the forest outline.

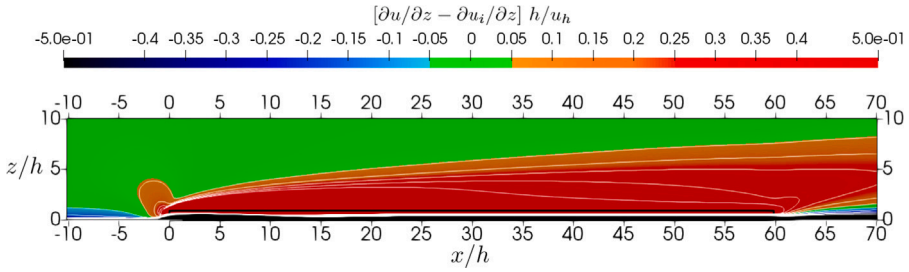

Fig. 12. Visualisation of the RSL height by the spatial distribution of the gradient deviation Δ_{RSL} at a vertical plane around the forest as in Fig. 11. The black rectangle represents the forest outline.

within the roughness sub-layer, and an additional high-intensity zone located downstream to the forest downwind edge, where turbulence is triggered by the interaction between the non-zero vertical and the streamwise velocity (TKE wake production).

Above the forest, the roughness sub-layer (RSL) develops. Following the method used in Bou-Zeid et al. (2004) and Dupont and Brunet (2009), the RSL depth can be determined by comparing the (non-dimensional) vertical gradient of the mean streamwise velocity u_x above the forest with the vertical gradient of the unperturbed atmospheric wind profile u_{atm} that impacts the forest:

$$\Delta_{RSL} = \frac{h}{u_h}\left(\frac{\partial u_x}{\partial z} - \frac{\partial u_{atm}}{\partial z}\right). \tag{22}$$

The RSL height is defined as the height Z_* at which the flow becomes not affected by the forest canopy efforts and it is determined as the height where the gradient deviation Δ_{RSL} is practically zero, i.e. $\Delta_{RSL}(Z_*) < 0.05$.

Fig. 12 shows the spatial distribution of Δ_{RSL} at a vertical plane around the forest. The RSL is characterised by positive values of the gradient deviation; it begins to develop on the upwind edge of the forest and rapidly increases its height, continuing to grow above the forest and beyond the end of the forest. As highlighted by Fig. 12, the higher level of the forest mast is located inside the RSL, justifying the observed behaviours of the wind-component fluctuations described by the quadrant analysis (see Section 3.1).

6.2. Regions of motions in streamwise direction

Following Belcher et al. (2012), at least three main regions of motion can be detected in a finite forest: The impact region, upwind to the forest edge where the atmospheric wind starts to be affected by the presence of the trees; the adjustment region, located in the forest and characterised by vertical velocities and transport; the canopy region, positioned immediately afterward where the internal forest flow profile stabilises.

In order to better understand the different regions of motion that characterise the internal dynamics of the forest flow, and to quantify the boundaries of such regions, the streamwise momentum budget is analysed:

$$0 = \underbrace{-u\frac{\partial u}{\partial x}}_{\mathrm{adv}_x} \underbrace{-w\frac{\partial u}{\partial z}}_{\mathrm{adv}_z} \underbrace{-\frac{1}{\rho}\frac{\partial p}{\partial x}}_{\mathrm{press}} \underbrace{+\frac{\partial}{\partial x}\left(\nu_{eff}\frac{\partial u}{\partial x}\right)}_{\mathrm{diff}_x} \underbrace{+\frac{\partial}{\partial z}\left(\nu_{eff}\frac{\partial u}{\partial z}\right)}_{\mathrm{diff}_z} \underbrace{-C_D\alpha|u|u}_{\mathrm{drag}}, \tag{23}$$

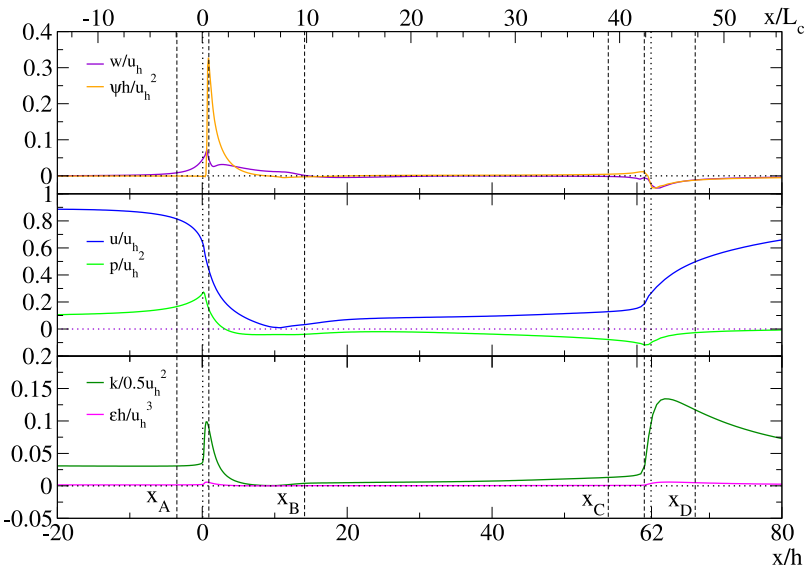

Fig. 13. In-forest profiles of several non-dimensional variables at horizontal line $z/h = 0.5$: Top panel, neutral condition parameter, and vertical velocity; centre panel, streamwise velocity and pressure; bottom panel, TKE and its dissipation.

where $\nu_{eff} = \nu + \nu_t$ is the effective viscosity and the various terms represent, respectively: The horizontal and vertical advection, the pressure force, the horizontal and vertical diffusion (both molecular and turbulent), and the forest drag. The magnitude of the various terms indicated which forces influence the flow at a given region.

In particular, in the canopy region, the flow is expected to be in a neutral condition, i.e. almost zero horizontal derivatives and vertical velocity (Massman, 1997). Under these assumptions Eq. (23) simplifies to:

$$\psi = \frac{\partial}{\partial z}\left(\nu_{eff}\frac{\partial u}{\partial z}\right) - C_D\alpha|u|u \tag{24}$$

where ψ is the in-canopy stability parameter which is here introduced. The regions in the forest where ψ is practically zero and the vertical velocity is negligible can be classified as internal regions, where the effects of the forest edges are minimal.

Fig. 13 shows several mean variables along a horizontal line at the forest mid-high ($z/h = 0.5$). The top panel presents the parameter ψ together with the vertical velocity w, which are utilised to determine the regions of the neutral condition. The central panel reports the streamwise velocity and pressure to investigate the in-forest flow dynamics. The bottom panel displays TKE and its dissipation. Two additional levels ($z/h = 2.5, 0.75$) have been analysed and show very similar features; hence, they are not reported. Seven regions of motion have been identified:

Inflow region: $x/h < x_A$, is the region upwind at the forest where the approaching wind is almost unperturbed. Vertical velocity and ψ are null, indicating a neutral condition, while streamwise velocity, pressure, and turbulent quantities tend to an asymptotic value for $x \ll x_A$.

Impact region: $x_A < x/h < x_i$ (where $x_i = 0$ is where the forest starts), the area upwind the forest edge where ψ is still zero, but a small vertical velocity appears. The approaching wind is slightly deviated upwards and reduces its intensity near the forest edge.

Impact-adjustment region: $x_i < x/h < x_B$, the region within the forest that is affected by edge effects. The ψ is non-zero and a weak vertical velocity is detectable; moreover, the pressure assumes small negative values, and the streamwise velocity decays to almost zero values. Near the forest edge ($x/h \sim 1$), it is detectable a peak of TKE and ϵ triggered by the strong drag generated by the forest canopy.

Table 5
Boundaries of the regions of motion for the case study under consideration made non-dimensional by the forest high h and the canopy drag length L_c. Approximation to decimal.

Location	x_A	x_B	x_C	x_D
x/h	−3.4	14	56	68
x/L_c	−2.4	10	39	46.5

Internal region: $x_B < x/h < x_C$, is the central region of the forest where the neutral condition is established. Both ψ and vertical velocity are null, and the profiles of velocity, TKE, and pressure assume almost constant values.

Exit-adjustment region: $x_C < x/h < x_f$ (where $x_f = 62$ is where forest finishes), the region affected by downwind forest edge effects. The parameter ψ assumes weak positive values and vertical velocity and pressure intensity increase.

Exit region: $x_f < x/h < x_D$, the region downwind of the forest edge is characterised by a negative vertical velocity, a rapid increase in streamwise velocity, together with TKE and ϵ, and a decrease in pressure. Also, vertical diffusion acts in this region.

Wake region: $x_D < x/h$, the region downwind of the forest where wake flow develops.

There is no clear consensus in the literature to determine the limits of regions of motion. The classification here proposed is based on the in-canopy stability parameter and the non-dimensional vertical velocity at the forest mid-high: The boundary of the regions are detected as the points in which both quantities are practically zero, i.e. $w/u_h < 0.01$ and $\psi < 0.01$. Table 5 reports the values of the points delimiting the various regions.

These criteria are partly discretionary and, for example, the impact region can be considered more extensive if one considers that the streamwise velocity and pressure profiles start deflecting already at $x/h = -10$. Analogously, the exit region can be considered more or less extended: Li et al. (1990) quantifies the exit region extension in around $8h$ from the edge, while Belcher et al. (2012) indicates an extension of $1h$. The definition of the exit-adjustment region is particularly delicate because the mean variables (u, k, p) show no clear

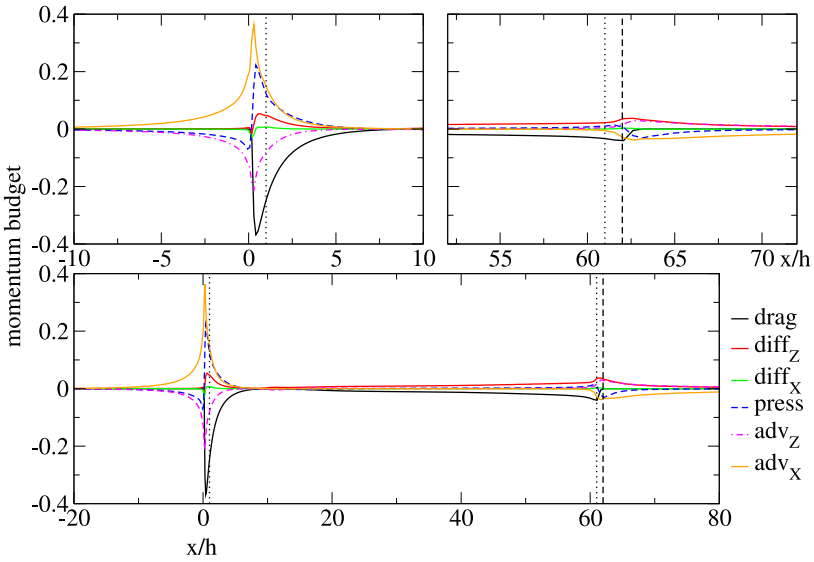

Fig. 14. Streamwise momentum budget at a horizontal line $x/h = 0.5$ (bottom panel), with a focus on the forest upwind edge (top left panel) and downwind edge (top right panel). Terms of Eq. (23) made non-dimensional by h/u_h^2.

discontinuities between the internal region and the exit-adjustment region; however, the non-zero values of the in-canopy stability parameter and the emergence of a weak vertical velocity suggested the identification of this additional region. Regarding the extension of the inflow adjustment region, Belcher et al. (2012) elaborates an estimation function for a homogeneous forest, which is based on forces balance: $x_B = c_B L_c \ln(hu_h/L_c u_*)$, where $c_B \sim 3$ from numerical simulations and u_* is the friction velocity in the overlying boundary layer. For a sparse forest ($h/L_c < 1$) $K \sim 1$ and, thus, in our case $x_B = 3L_c \sim 4.5h$; which is a lower estimation than the one provided here.

Fig. 14 shows the streamwise momentum budget at the horizontal line at the forest mid-high, with a zoom near the upwind and downwind forest edge. In the impact region, high positive values of horizontal advection arise along with negative pressure force and vertical advection, as a consequence of the obstacle to motion generated by the forest edge. In the impact-adjustment region, a strong negative drag force is mainly balanced by positive horizontal advection and pressure gradient, which drives the flow within the canopy. In the internal region, when the flow stream in the forest more easily, pressure and advective terms decay to zero and the drag force is balanced by vertical diffusion. In the exit region, the horizontal advection becomes negative and replaces the drag force outside the forest in balancing the vertical diffusion, together with a negative pressure gradient. This may indicate a suction effect downwind to the forest.

6.3. Flow layers along the vertical direction

The forest flow is further investigated by discussing the mean and turbulent quantities along vertical lines. Fig. 15 presents non-dimensional velocity components, k and ϵ along six vertical lines placed at the centre of the regions of motion identified: $x/h = -1.5, 7, 35, 59, 65$, plus $x/h = -20$ where the atmospheric wind is almost unperturbed. Streamwise velocity profiles practically collapse on the same curve approximately at $z/h > 6$. Above the canopy ($1 < z/h < 6$) the roughness sub-layer develops: in the impact-adjustment region, velocity rapidly decays to small values at $z/h = 2.5$, while the profiles in the subsequent regions are similar and show lower velocities. In the canopy sub-layer ($0 < z/h < 1$), two additional layers can be detected:

Foliage layer: ($0.5 < z/h < 1$), is the region where velocity is drastically reduced because of the drag force, which is more intense due to the higher values of LAD;

Bush layer: ($0 < z/h < 0.5$), is the region where the less dense vegetation found in the undergrowth is reproduced by a smaller LAD. This allows a higher velocity, which shows a local peak near the ground.

The presence and extent of these two layers are dependent on the choice of LAD profile and C_D. In general, the LAD profile for modelling a vertically non-homogeneous canopy has high values at the top and low ones at the bottom, which supports the development of these two layers. In the foliage layer, the streamwise velocity increases for increasing values of x/h. In the bush layer, the velocity peak is lower in the internal region while it is higher in the impact and exit-adjustment regions, which are more influenced by edge effects. In the exit region, velocity assumes an almost linear profile at the forest level. Vertical velocity assumes small positive values in the impact and impact-adjustment regions, indicating a weak upward motion, while it is almost null in the internal region, as expected. Conversely, in the exit adjustment and exit regions, negative values are detectable, suggesting a weak downward flow. This is in agreement with the momentum budget in Fig. 14. This dynamic is similar to that which is generated around a solid obstacle, characterised by a weak upward motion in the upwind area and a downward motion in the downwind area.

The TKE exhibits almost zero values in the bush layer, possibly because of the low velocities, and a rapid increase in the foliage layer as a consequence of the increasing velocity and the interaction with the overlying wind. The profiles within the canopy practically collapse on each other. The TKE peaks in the roughness sub-layer (in the range $1 < z/h < 2$) and the profile extends more in the vertical direction for increasing x/h. TKE dissipation follows a similar behaviour; it is worth noticing that ϵ peaks at the same height above the forest ($z/h \sim 1.25$) and that larger values are produced in the impact-adjustment region. The profile above the peak ($z/h > 12.5$) remains almost unaltered in the downstream regions.

As already guessed from the quadrant analysis (see Section 3.1), the forest canopy shows clear dynamic differences with the elevation. The direct link with the vertical distributions of LAD and foliage drag, as well as the different forcing applied to the flow within bush and foliage layers, is here magnified and observed to evolve in the $x-$direction. Fig. 16 reports the streamwise momentum budget and TKE budget along three selected vertical lines located near the forest edge ($x/h = 2$), in the internal region at the forest mast location ($x/h = 31$), in the exit region ($x/h = 63$). The TKE budget is given in Eq. (7), where

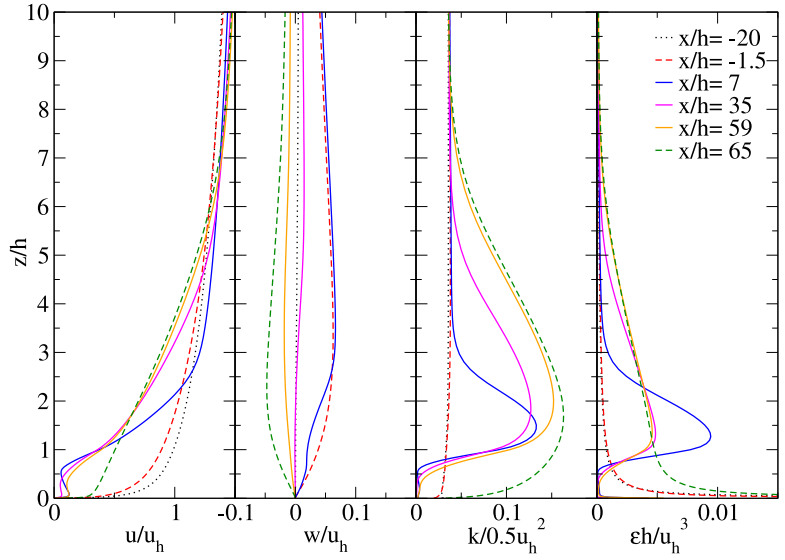

Fig. 15. Non-dimensional velocity component, TKE and its dissipation at six selected locations at the centre of the identified motion regions. Dashed lines are located outside the forest, solid lines intercept the forest canopy.

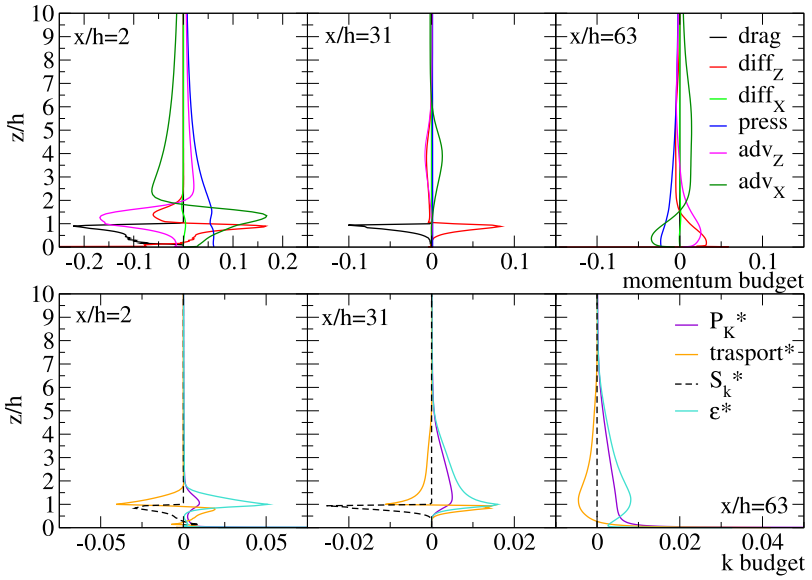

Fig. 16. Streamwise momentum budget (top panel) and TKE budget (bottom panel) at selected vertical lines: $x/h = 2, 31, 63$. Terms of Eq. (23) made non-dimensional by h/u_h^2. The terms of k budget are marked with an asterisk because they are made non-dimensional by h/u_h^2, see Eq. (7).

the transport term combines the terms diffusion and advection. The streamwise momentum budget at $x/h = 2$ shows that in the canopy layer, the drag force is primarily balanced by vertical diffusion. Both peak at the forest top ($z/h = 1$) and exhibit a decrease in intensity in the bush layer. In the impact adjustment region, a positive pressure gradient supports the flow penetration into the canopy together with a horizontal advection, which reaches the maximum above the canopy at $z/h \sim 1.5$. At this height, it is balanced by negative horizontal advection and diffusion. In the range $1 < z/h < 2$, the roughness sublayer develops as shown in Fig. 12: It exhibits weak positive horizontal advection and negative vertical diffusion and advection. This feature is a characteristic of the RSL above the forest and can be found also in the internal region $x/h = 31$ at level $1 < z/h < 6$. Above $z/h = 2$, the driving forces are pressure and advection. At $x/h = 31$, the flow is in a neutral condition: Drag and vertical diffusion balance in the foliage layer. At $x/h = 63$, a negative pressure gradient and horizontal advection are generated on the downwind side of the forest edge and balanced by horizontal diffusion and advection. Above the forest canopy, a positive horizontal advection can be highlighted.

Fig. 17a shows the velocity streamlines within and around the forest. In the impact-adjustment region, the flow is deviated upwards by the forest canopy, while in the exit region it smoothly deviates downwards. By continuity, the upward deviation generates a weak backflow confined in the bush layer, which drains air from the internal region in the opposite direction to the main wind, taking advantage of the reduced drag in this layer. As a result, a recirculation cell appears between the impact-adjustment region and the internal region. Fig. 17b,c display, respectively, the velocity components profiles along a horizontal line at the mid-height level of the bush layer and at a vertical line at the boundary of the internal region, which is approximately coincident with the centre of the recirculation cell. Such a cell extends horizontally in the range $10 < x/h < 20$, where negative values of streamwise velocity are detected. This is in agreement with literature results, e.g. Cassiani et al. (2008). Surprisingly, the vertical

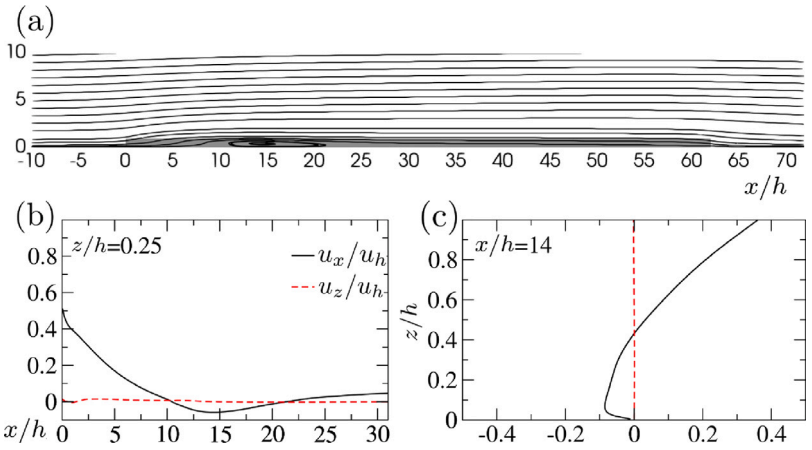

Fig. 17. Visualisation of the recirculation region in the bush layer: (a) Velocity streamlines; (b) Non-dimensional streamwise and vertical velocity components at a horizontal line $z/h = 0.25$ (bush layer mid-height); (c) Non-dimensional streamwise and vertical velocity components at a vertical line $x/h = 14$ (the boundary between the impact-adjustment region and the internal region).

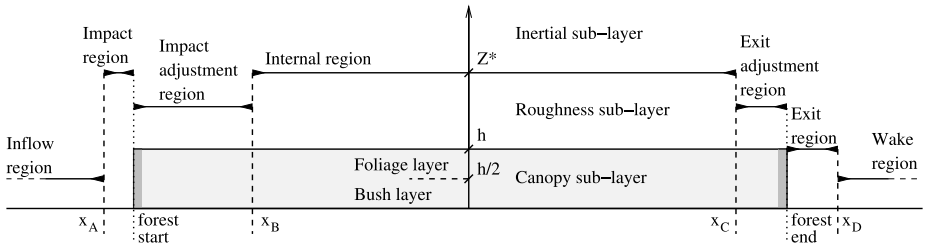

Fig. 18. Sketch of the regions of motion and vertical flow layers characterising the air dynamics in a finite forest with a vertically non-homogeneous canopy. This is an improved version of the original one proposed by Belcher et al. (2012). See Table 5 for boundary values.

velocity is almost null. The backflow maximum velocity is $u_{max}/u_h \sim -0.9$. The presence of the recirculation cell has been detected by Dalpé and Masson (2009), which pointed out that its location, extension and intensity are dependent on the LAD profile and the C_D parameter of the forest canopy. In this concern, Cassiani et al. (2008) proposed a simplified analytical function to estimate the location x_R of the starting point of the recirculation zone. This reads:

$$x_R/h = \frac{2a+1}{C_D\lambda}\frac{p_0}{u_0^2} \tag{25}$$

where $a \geq 2$ is an unknown parameter and p_0, u_0 are the pressure and velocity values (respectively) at the inlet near the ground ($z/h < 0.1$). Following the suggestion of the authors, the model parameter is set to $a = 2$ giving $x_R/h = 3.7$ which underestimates the recirculation-zone starting point; setting $a = 7$ the model estimates $x_R/h = 11.14$ which is in line with the observations. Hence, the uncertainty about the value of a may limit the predicting ability of this function.

7. Summary and conclusions

The present study investigates the internal ventilation of a finite forest with a vertically non-homogeneous canopy. The case study under consideration is that of 'Bosco Fontana', located in the north of Italy. An experimental campaign was conducted in the forest and resulted in a dataset with which the turbulent exchanges along the vertical in the inner region of the forest are investigated. Subsequently, the case study is reproduced by means of a Reynolds-Averaged Navier–Stokes numerical simulation, that is successfully validated against the experimental dataset and analytical results present in the literature.

The study allowed careful analysis of the ventilation inside the forest. A new in-canopy stability parameter ψ was introduced to delimit the horizontal regions of motion in a finite forest, while characterisation of the canopy layer was proposed in the case of vertically non-homogeneous canopies. The outcome allows us to expand the classification given in Belcher et al. (2012) for a homogeneous forest, introducing novel dynamic layers and regions of motion for a non-homogeneous canopy as framed in Fig. 18. This novel classification refines the characterisation of wind dynamics close to the forest edges, where the flow is adjusted to the pressure field exerted by the forest, and within the canopy, where the vertically non-homogeneous foliage distribution impacts the vertical exchanges. In the vertical direction, three classical dynamic layers arise: inertial, roughness, and canopy sub-layers. Given that the canopy is vertically non-homogeneous, it is additionally divided into a foliage layer, where the drag effects due to leaves are more effective, and a bush layer, where the sink of momentum is weaker. The former is characterised by an increase of streamwise velocity, TKE and its dissipation, sustained by an even distribution of vertical and horizontal velocity fluctuations; drag force is more intense and mainly balanced by a horizontal diffusion of momentum; at the top of this layer, the predominance of a downward turbulent momentum transport from the roughness sub-layer drives air intrusion from above the forest or the formation of recirculation zones at the canopy top. The latter exhibits weak horizontal velocity and develops a characteristic backflow at the boundary between the impact-adjustment region and the internal region, possibly sustained by the downward momentum transport caused by frequent and intense sweep events. The height of the two layers possibly depends on the LAD profile and the drag coefficient C_D. In the horizontal direction, seven regions of motion are detected. The area upwind to the forest is characterised by an inflow region, where the atmospheric wind is almost unperturbed, and an impact region close to the forest edge, where the wind velocity is reduced and the flow deviates above the forest. Within the forest, three

main regions are identified in the foliage layer: An impact-adjustment region where a pressure change of sign and streamwise velocity rapidly decrease, while a vertical velocity appears and drives the flow towards the forest top boundary. The interaction of the main flow with the canopy triggers a high level of turbulence (quantify by a peak of TKE). The limit of this region x_B is identified when both the newly introduced in-canopy stability parameter and the vertical velocity vanish, suggesting the establishment of a dynamic equilibrium that characterises the subsequent internal region. Such a parameter is an attempt to establish a clear criterion to determine x_B from the in-canopy airflow variables and which, to the best of the author's knowledge, is missing. In the internal region, velocity is mainly directed horizontally and does not vary significantly in intensity. In the momentum budget, the canopy drag force is balanced by vertical diffusion and the level of TKE is stable in a streamwise direction. Near the end of the forest, an exit-adjustment region is detected, where the in-forest velocity is slightly deviated downwards and increases in intensity in the streamwise direction. The area downwind to the forest edge is characterised by the exit region where TKE peaks, streamwise velocity rapidly increases, and is weakly deflected downwards near the ground. Subsequently, the wake region is established.

Although constrained to a condition of near-neutral stability, the present novel classification gives a more exhaustive picture of the complex interaction between the wind field and vertical non-homogeneous forest canopies. It represents a purely aerodynamic classification, depicting a baseline behaviour driven by mechanical processes and the canopy roughness. In such terms, it provides an exploitable tool for mechanically-driven forest characterisation. Possible future developments include the introduction of a pollution source to investigate how the forest interacts with its dispersion, as well as the incorporation of thermal effects and in particular the stable or unstable stratification of the atmosphere, common in real-world configurations.

Declaration of competing interest

The authors declare that they have no known competing financial interests or personal relationships that could have appeared to influence the work reported in this paper.

Data availability

Data will be made available on request.

Acknowledgments

This research project is implemented under the National Recovery and Resilience Plan (NRRP), Project title "National Biodiversity Future Center - NBFC", CUP J33C22001190001. Università Cattolica del Sacro Cuore also contributed to the publication of this research. The authors are greatful to Ph.D. Laura Bignotti for her precious help during the field campaign.

References

Antonia, R.A., Chambers, A.J., Satyaprakash, B.R., 1981. Reynolds number dependence of high-order moments of the streamwise turbulent velocity derivative. Bound.-Lay. Meteorol. 21 (2), 159–171. http://dx.doi.org/10.1007/BF02033934.

Arya, P., 1998. Introduction to Micrometeorology. In: International Geophysics Series, Academic Press.

Bailey, B.N., Stoll, R., 2013. Turbulence in sparse, organized vegetative canopies: A large-eddy simulation study. Bound.-Lay. Meteorol. 147, 369–400.

Baldocchi, D.D., Hutchinson, B.A., 1987. Turbulence in an almond Orchard: Vertical variation in turbulence statistics. Bound.-Lay. Meteorol. 40 (1–2), 127–146. http://dx.doi.org/10.1007/BF00121712.

Banerjee, T., Brugger, P., De Roo, F., Kröniger, K., Yakir, D., Rotenberg, E., Mauder, M., 2018. Turbulent transport of energy across a forest and a semiarid shrubland. Atmos. Chem. Phys. 18 (13), 10025–10038.

Banerjee, T., De Roo, F., Mauder, M., 2017. Explaining the convector effect in canopy turbulence by means of large-eddy simulation. Hydrol. Earth Syst. Sci. 21 (6), 2987–3000.

Banerjee, T., Katul, G., Fontan, S., Poggi, D., Kumar, M., 2013. Mean flow near edges and within cavities situated inside dense canopies. Bound.-Lay. Meteorol. 149 (1), 19–41.

Barbano, F., Brattich, E., Di Sabatino, S., 2021. Characteristic scales for turbulent exchange processes in a real urban canopy. Bound.-Lay. Meteorol. 178, 119–142.

Belcher, S.E., Finnigan, J.J., Harman, I.N., 2008. Flows through forest canopies in complex terrain. Ecol. Appl. 18 (6), 1436–1453. http://dx.doi.org/10.1890/06-1894.1.

Belcher, S.E., Harman, I.N., Finnigan, J.J., 2012. The wind in the Willows: Flows in forest canopies in complex terrain. Annu. Rev. Fluid Mech. 44, 479—504. http://dx.doi.org/10.1146/annurev-fluid-120710-101036.

Belcher, S., Jerram, N., Hunt, J., 2003. Adjustment of a turbulent boundary layer to a canopy of roughness elements. J. Fluid Mech. 488, 369–398.

Bohrer, G., Katul, G.G., Walko, R.L., Avissar, R., 2009. Exploring the effects of microscale structural heterogeneity of forest canopies using large-eddy simulations. Bound.-Lay. Meteorol. 132, 351–382.

Bou-Zeid, E., Meneveau, C., Parlange, M.B., 2004. Large-eddy simulation of neutral atmospheric boundary layer flow over heterogeneous surfaces: blending height and effective surface roughness. Water Resour. Res. 40 (2), http://dx.doi.org/10.1029/2003WR002475, W02505.

Boudreault, L.-É., Dupont, S., Bechmann, A., Dellwik, E., 2017. How forest inhomogeneities affect the edge flow. Bound.-Lay. Meteorol. 162 (3), 375–400.

Brunet, Y., 2020. Turbulent flow in plant canopies: Historical perspective and overview. Bound.-Lay. Meteorol. 177 (2–3), 315–364.

Cassiani, M., Katul, G., Albertson, J., 2008. The effects of canopy leaf area index on airflow across forest edges: Large-eddy simulation and analytical results. Bound.-Lay. Meteorol. 126, 433–460.

Chiesa, M., Bignotti, L., Finco, A., Marzuoli, R., Gerosa, G., 2019. Size-resolved aerosol fluxes above a broadleaved deciduous forest. Agricult. Forest Meteorol. 279, 107757. http://dx.doi.org/10.1016/j.agrformet.2019.107757.

Christen, A., Vogt, R., 2004. Direct measurement of dispersive fluxes within a cork oak plantation. In: Proceedings of 26th Conference on Agricultural and Forest Meteorology. American Meteorological Society.

Cintolesi, C., Barbano, F., Di Sabatino, S., 2021a. Large-eddy simulation analyses of heated urban canyon facades. Energies 14 (11), 3078.

Cintolesi, C., Pulvirenti, B., Di Sabatino, S., 2021b. Large-eddy simulations of pollutant removal enhancement from urban canyons. Boundary-Layer Meteorology 180, 79–104.

Cionco, R.M., 1965. A mathematical model for air flow in a vegetative canopy. J. Appl. Meteorol. 4, 517–522. http://dx.doi.org/10.1016/j.agrformet.2019.107757.

Clark, T.L., Mitchell, S.J., Novak, M., 2007. Three-dimensional simulations and wind-tunnel experiments on airflow over isolated forest stands. Bound.-Lay. Meteorol. 125, 487–503.

Clausnitzer, F., Köstner, B., Schwärzel, K., Bernhofer, C., 2011. Relationships between canopy transpiration, atmospheric conditions and soil water availability—Analyses of long-term sap-flow measurements in an old Norway spruce forest at the ore mountains/Germany. Agricult. Forest Meteorol. 151 (8), 1023–1034.

Dalpé, B., Masson, C., 2009. Numerical simulation of wind flow near a forest edge. J. Wind Eng. Ind. Aerodyn. 97, 228–241. http://dx.doi.org/10.1016/j.jweia.2009.06.008.

Dalponte, M., Bruzzone, L., Gianelle, D., 2008. Fusion of hyperspectral and LIDAR remote sensing data for classification of Complex Forest Areas. IEEE Trans. Geosci. Remote Sens. 46 (5), 1416–1427. http://dx.doi.org/10.1109/TGRS.2008.916480.

Dellwik, E., Bingöl, F., Mann, J., 2014. Flow distortion at a dense forest edge. Q. J. R. Meteorol. Soc. 140 (679), 676–686.

Desmond, C.J., Watson, S.J., Aubrun, S., Avila, S., Hancock, P., Sayer, A., 2014. A study on the inclusion of forest canopy morphology data in numerical simulations for the purpose of wind resource assessment. J. Wind Eng. Ind. Aerodyn. 126, 24–37.

Dupont, S., Bonnefond, J.-M., Irvine, M.R., Lamaud, E., Brunet, Y., 2011a. Long-distance edge effects in a pine forest with a deep and sparse trunk space: In situ and numerical experiments. Agricult. Forest Meteorol. 151 (3), 328–344.

Dupont, S., Bonnefond, J.-M., Irvine, M.R., Lamaud, E., Brunet, Y., 2011b. Long-distance edge effects in a pine forest with a deep and sparse trunk space: In situ and numerical experiments. Agricult. Forest Meteorol. 151 (3), 328–344.

Dupont, S., Brunet, Y., 2009. Coherent structures in canopy edge flow: A large-eddy simulation study. J. Fluid Mech. 630, 93–128. http://dx.doi.org/10.1017/S0022112009006739.

Dupont, S., Irvine, M.R., Bonnefond, J.-M., Lamaud, E., Brunet, Y., 2012. Turbulent structures in a pine forest with a deep and sparse trunk space: Stand and edge regions. Bound.-Lay. Meteorol. 143, 309–336. http://dx.doi.org/10.1007/s10546-012-9695-8.

Eder, F., Serafimovich, A., Foken, T., 2013. Coherent structures at a forest edge: properties, coupling and impact of secondary circulations. Bound.-Lay. Meteorol. 148 (2), 285–308.

Finnigan, J., 2000. Turbulence in plant canopies. Annu. Rev. Fluid Mech. 32 (1), 519–571.

Finnigan, J.J., Shaw, R.H., Patton, E.G., 2009. Turbulence structure above a vegetation canopy. J. Fluid Mech. 637, 387–424. http://dx.doi.org/10.1017/S0022112009990589.

Flerchinger, G.N., Reba, M.L., Link, T.E., Marks, D., 2015. Modeling temperature and humidity profiles within forest canopies. Agricult. Forest Meteorol. 213, 251–262. http://dx.doi.org/10.1016/j.agrformet.2015.07.007, URL https://www.sciencedirect.com/science/article/pii/S0168192315002142.

Gardiner, B.A., 1994. Wind and wind forces in a plantation spruce forest. Bound.-Lay. Meteorol. 67, 161—186.

Garratt, J., 1994. The Atmospheric Boundary Layer. In: Cambridge Atmospheric and Space Science Series, Cambridge University Press, URL https://books.google.it/books?id=xeEVtBRApAkC.

Gavrilov, K., Accary, G., Morvan, D., Lyubimov, D., Méradji, S., Bessonov, O., 2011. Numerical simulation of coherent structures over plant canopy. Flow Turbul. Combust. 86, 89–111. http://dx.doi.org/10.1007/s10494-010-9294-z.

Gerosa, G., Marzuoli, R., Monteleone, B., Chiesa, M., Finco, A., 2017. Vertical ozone gradients above forests. Comparison of different calculation options with direct ozone measurements above a mature forest and consequences for Ozone risk assessment. Forests 8 (9), http://dx.doi.org/10.3390/f8090337, URL https://www.mdpi.com/1999-4907/8/9/337.

Gromke, C., 2018. Wind tunnel model of the forest and its Reynolds number sensitivity. J. Wind Eng. Ind. Aerodyn. 175, 53–64. http://dx.doi.org/10.1016/j.jweia.2018.01.036.

Gross, G., 2012. Numerical Simulation of Canopy Flows, Vol. 12. Springer Science & Business Media, http://dx.doi.org/10.1007/978-3-642-75676-4.

Harman, I.N., Finnigan, J.J., 2007. A simple unified theory for flow in the canopy and roughness sublayer. Bound.-Lay. Meteorol. 123, 339–363. http://dx.doi.org/10.1007/s10546-006-9145-6.

Jimenez, J., Cogollos, M., Bernal, L.P., 1985. A perspective view of the plane mixing layer. J. Fluid Mech. 152, 125–143. http://dx.doi.org/10.1017/S002211208500060X.

Jonckheere, I., Fleck, S., Nackaerts, K., Muys, B., Coppin, P., Weiss, M., Baret, F., 2004. Review of methods for in situ leaf area index determination: Part I. theories, sensors and hemispherical photography. Agricult. Forest Meteorol. 121 (1–2), 19–35.

Kaimal, J.C., Finnigan, J.J., 1994. Atmospheric Boundary Layer Flows: Their Structure and Measurement. Oxford University Press, http://dx.doi.org/10.1002/qj.49712152512.

Kanani-Sühring, F., Raasch, S., 2015. Spatial variability of scalar concentrations and fluxes downstream of a clearing-to-forest transition: A large-eddy simulation study. Bound.-Lay. Meteorol. 155 (1), 1–27.

Katul, G.G., Mahrt, L., Poggi, D., Sanz, C., 2004. ONE- and TWO-equation models for canopy turbulence. Bound.-Lay. Meteorol. 113, 81–109. http://dx.doi.org/10.1023/B:BOUN.0000037333.48760.

Klaassen, W., Sogachev, A., 2006. Flux footprint simulation downwind of a forest edge. Bound.-Lay. Meteorol. 121 (3), 459–473.

Klaassen, W., Van Breugel, P., Moors, E., Nieveen, J., 2002. Increased heat fluxes near a forest edge. Theor. Appl. Climatol. 72 (3), 231–243.

Kormas, A., Prospathopoulos, J., Chaviaropoulos, P., Yakinthos, K., 2016. Wind flow simulation over forested areas using a 3D RANS solver with a tree–scale approach. J. Wind Eng. Ind. Aerodyn. 155, 149–158.

Kruijt, B., Malhi, Y., Lloyd, J., Norbre, A.D., Miranda, A.C., Pereira, M.G.P., Culf, A., Grace, J., 2000. Turbulence statistics above and within two Amazon rain forest canopies. Bound.-Lay. Meteorol. 94, 297–331. http://dx.doi.org/10.1023/A:1002401829007.

Lalic, B., Mihailovic, D.T., 2004. An empirical relation describing leaf-area density inside the forest for environmental modeling. J. Appl. Meteorol. 43 (4), 641–645. http://dx.doi.org/10.1175/1520-0450(2004)043<0641:AERDLD>2.0.CO;2.

Launder, B., Spalding, D., 1974. The numerical computation of turbulent flows. Comput. Methods Appl. Mech. Engrg. 3 (2), 269–289. http://dx.doi.org/10.1016/0045-7825(74)90029-2.

Launiainen, S., Vesala, T., Mölder, M., Mammarella, I., Smolander, S., Rannik, U., Kolari, P., Hari, P., Lindroth, A., Katul, G., 2007. Vertical variability and effect of stability on turbulence characteristics down to the floor of a pine forest. Tellus B 59, http://dx.doi.org/10.3402/tellusb.v59i5.17070.

Leuning, R., Cleugh, H.A., Zegelin, S.J., Hughes, D., 2005. Carbon and water fluxes over a temperate eucalyptus forest and a tropical wet/dry savanna in Australia: Measurements and comparison with MODIS remote sensing estimates. Agricult. Forest Meteorol. 129 (3–4), 151–173.

Li, Z., Lin, J., Miller, D., 1990. Air flow over and through a forest edge: A steady-state numerical simulation. Bound.-Lay. Meteorol. 51 (1), 179–197.

Lopes, A.S., Palma, J., Lopes, J.V., 2016. Modelling flows within forested areas using the k—ϵ RaNS model. J. Phys. Conf. Ser. 753 (8), 082035.

Ma, Y., Liu, H., Banerjee, T., Katul, G.G., Yi, C., Pardyjak, E.R., 2020. The effects of canopy morphology on flow over a two-dimensional isolated ridge. J. Geophys. Res.: Atmos. 125 (19), e2020JD033027.

Massman, W., 1997. An analytical one-dimensional model of momentum transfer by vegetation of arbitrary structure. Bound.-Lay. Meteorol. 83, 407–421. http://dx.doi.org/10.1023/A:1000234813011.

McMillen, R., 1988. An eddy correlation technique with extended applicability to non-simple terrain. Boundary-Layer Meteorol. 43 (3), 231–245.

Morales Garza, V.G., Sumner, J., Nathan, J., Masson, C., 2019a. Evaluating the accuracy of RANS wind flow modeling over forested terrain—Part 1: Canopy model validation. J. Solar Energy Eng. 141 (4).

Morales Garza, V.G., Sumner, J., Nathan, J., Masson, C., 2019b. Evaluating the accuracy of RANS wind flow modeling over forested terrain. Part 2: Impact on capacity factor for moderately complex topography. J. Solar Energy Eng. 142 (2), http://dx.doi.org/10.1115/1.4045145, 021006.

Morse, A., Gardiner, B., Marshall, B., 2002. Mechanisms controlling turbulence development across a forest edge. Bound.-Lay. Meteorol. 103 (2), 227–251.

Mueller, E., Mell, W., Simeoni, A., 2014. Large eddy simulation of forest canopy flow for wildland fire modeling. Can. J. Forest Res. 44 (12), 1534–1544.

Nakagawa, H., Nezu, I., 1977. Prediction of the contributions to the Reynolds stress from bursting events in open-channel flows. J. Fluid Mech. 80 (1), 99–128. http://dx.doi.org/10.1017/S0022112077001554.

OpenFOAM version 6.0, 2019. The OpenFOAM foundation. http://openfoam.org (Accessed: 1 May 2019).

Pan, Y., Chamecki, M., Isard, S.A., Nepf, H.M., 2015. Dispersion of particles released at the leading edge of a crop canopy. Agricult. Forest Meteorol. 211, 37–47.

Poggi, D., Porporato, A., Ridolfi, L., Albertson, J., Katul, G.G., 2004. The effect of vegetation density on canopy SubLayer turbulence. Bound.-Lay. Meteorol. 111, 565–587. http://dx.doi.org/10.1023/B:BOUN.0000016576.05621.73.

Rannik, Ü., Markkanen, T., Raittila, J., Hari, P., Vesala, T., 2003. Turbulence statistics inside and over forest: Influence on footprint prediction. Bound.-Lay. Meteorol. 109, 163–189. http://dx.doi.org/10.1023/A:1025404923169.

Raupach, M.R., 1981. Conditional statistics of Reynolds stress in rough-wall and smooth-wall turbulent boundary layers. J. Fluid Mech. 108, 363–382. http://dx.doi.org/10.1017/S0022112081002164.

Raupach, M.R., Coppin, P.A., Legg, B.J., 1986. Experiments on scalar dispersion within a model plant canopy part I: The turbulence structure. Bound.-Lay. Meteorol. 35, 21—52. http://dx.doi.org/10.1007/BF00117300.

Raupach, M.R., Finnigan, J.J., Brunei, Y., 1996. Coherent eddies and turbulence in vegetation canopies: The mixing-layer analogy. Bound.-Lay. Meteorol. 78, 351—382. http://dx.doi.org/10.1007/BF00120941.

Richards, P.J., Hoxey, R.P., 1993. Appropriate boundary conditions for computational wind engineering models using the $k-\epsilon$ turbulence model. J. Wind Eng. Ind. Aerodyn. 46–47, 145–153. http://dx.doi.org/10.1016/0167-6105(93)90124-7.

Sanz, C., 2003. A note on k - ϵ modelling of vegetation canopy air-flows. Bound.-Lay. Meteorol. 108, 191–197. http://dx.doi.org/10.1023/A:1023066012766.

Schlegel, F., Stiller, J., Bienert, A., Maas, H.-G., Queck, R., Bernhofer, C., 2012. Large-eddy simulation of inhomogeneous canopy flows using high resolution terrestrial laser scanning data. Bound.-Lay. Meteorol. 142, 223–243.

Schlegel, F., Stiller, J., Bienert, A., Maas, H.-G., Queck, R., Bernhofer, C., 2015. Large-eddy simulation study of the effects on flow of a heterogeneous forest at sub-tree resolution. Bound.-Lay. Meteorol. 154, 27–56.

Segersson, D., 2017. A tutorial to urban wind flow using OpenFOAM. Available at http://www.tfd.chalmers.se/~hani/kurser/OS_CFD/#YEAR_2017 (Accessed: 15 Feb 2020).

Shaw, R., Den Hartog, G., Neumann, H., 1988. Influence of foliar density and thermal stability on profiles of Reynolds stress and turbulence intensity in a deciduous forest. Bound.-Lay. Meteorol. 45, 391–409.

Shaw, R.H., Patton, E.G., 2003. Canopy element influences on resolved-and subgrid-scale energy within a large-eddy simulation. Agricult. Forest Meteorol. 115 (1–2), 5–17.

Shaw, R.H., Schumann, U., 1992. Large-eddy simulation of turbulent flow above and within a forest. Bound.-Lay. Meteorol. 61 (1–2), 47–64.

Shi, L., Yeo, D., 2016. OpenFOAM large-eddy simulations of atmospheric boundary layer turbulence for wind engineering applications. In: Technical Note (NIST TN). National Institute of Standards and Technology, Gaithersburg, MD, http://dx.doi.org/10.6028/NIST.TN.1944.

Sogachev, A., Leclerc, M., Karipot, A., Zhang, G., Vesala, T., 2005. Effect of clearcuts on footprints and flux measurements above a forest canopy. Agricult. Forest Meteorol. 133 (1–4), 182–196.

Sogachev, A., Leclerc, M.Y., Zhang, G., Rannik, Ü., Vesala, T., 2008. CO2 fluxes near a forest edge: A numerical study. Ecol. Appl. 18 (6), 1454–1469.

Stoy, P.C., Mauder, M., Foken, T., Marcolla, B., Boegh, E., Ibrom, A., Arain, M.A., Arneth, A., Aurela, M., Bernhofer, C., et al., 2013. A data-driven analysis of energy balance closure across FLUXNET research sites: The role of landscape scale heterogeneity. Agricult. Forest Meteorol. 171, 137–152.

Su, H.-B., Shaw, R.H., Paw, K.T., Moeng, C.-H., Sullivan, P.P., 1998. Turbulent statistics of neutrally stratified flow within and above a sparse forest from large-eddy simulation and field observations. Bound.-Lay. Meteorol. 88, 363–397.

Svensson, U., Häggkvist, K., 1990. A two-equation turbulence model for canopy flows. J. Wind Eng. Ind. Aerodyn. 35, 201–211. http://dx.doi.org/10.1016/0167-6105(90)90216-Y.

Vickers, D., Mahrt, L., 1997. Quality control and flux sampling problems for tower and aircraft data. J. Atmos. Ocean. Technol. 14 (3), 512–526. http://dx.doi.org/10.1175/1520-0426(1997)014<0512:QCAFSP>2.0.CO;2.

Wei, S., Yin, T., Dissegna, M.A., Whittle, A.J., Ow, G.L.F., Yusof, M.L.M., Lauret, N., Gastellu-Etchegorry, J.-P., 2020. An assessment study of three indirect methods for estimating leaf area density and leaf area index of individual trees. Agricult. Forest Meteorol. 292, 108101.

Yan, G., Hu, R., Luo, J., Weiss, M., Jiang, H., Mu, X., Xie, D., Zhang, W., 2019. Review of indirect optical measurements of leaf area index: Recent advances, challenges, and perspectives. Agricult. Forest Meteorol. 265, 390–411.

Yang, Y., Gu, M., Chen, S., Jin, X., 2009. New inflow boundary conditions for modelling the neutral equilibrium atmospheric boundary layer in computational wind engineering. J. Wind Eng. Ind. Aerodyn. 97, 88–95. http://dx.doi.org/10.1016/j.jweia.2008.12.001.

Yang, B., Morse, A.P., Shaw, R.H., Paw U, K.T., 2006a. Large-eddy simulation of turbulent flow across a forest edge. Part II: momentum and turbulent kinetic energy budgets. Bound.-Lay. Meteorol. 121, 433–457.

Yang, B., Raupach, M.R., Shaw, R.H., U, K.T.P., Morse, A.P., 2006b. Large-eddy simulation of turbulent flow across a forest edge. Part I: flow statistics. Bound.-Lay. Meteorol. 120, 377–412.

Yue, W., Meneveau, C., Parlange, M.B., Zhu, W., van Hout, R., Katz, J., 2007. A comparative quadrant analysis of turbulence in a plant canopy. Water Resour. Res. 43 (5).